Title	Stability of PdxOy Particles Supported on Strontium Titanate Perovskite under Three-Way Catalyst Operating Conditions: Implications for Sintering Resistance
Author(s)	Pham, Thanh Ngoc; Andrea Choi Tan, Beatriz; Hamamoto, Yuji et al.
Citation	ACS Catalysis. 2024, 14(3), p. 1443-1458
Version Type	AM
URL	https://hdl.handle.net/11094/93899
rights	This document is the Accepted Manuscript version of a Published Work that appeared in final form in ACS Catalysis, © American Chemical Society after peer review and technical editing by the publisher. To access the final edited and published work see https://doi.org/10.1021/acscatal.3c05673.
Note	

Stability of Pd_xO_y particles supported on strontium titanate perovskite under three-way catalyst operating conditions: Implications for sintering resistance

Thanh Ngoc Pham,[*,†] Beatriz Andrea Choi Tan,[†] Yuji Hamamoto,[†] Kouji Inagaki,[†] Ikutaro Hamada,[†] and Yoshitada Morikawa[*,†,‡]

†*Department of Precision Engineering, Graduate School of Engineering, Osaka University, 2-1, Yamada-oka, Suita, Osaka 565-0871, Japan*

‡*Research Center for Precision Engineering, Graduate School of Engineering, Osaka University, 2-1 Yamada-oka, Suita 565-0871, Osaka, Japan*

E-mail: thanh@cp.prec.eng.osaka-u.ac.jp; morikawa@prec.eng.osaka-u.ac.jp

Abstract

Self-regenerative materials are keys to the development of stable catalysts used under high temperature condition, e.g., three-way catalyst converters in automobiles. Among others, metal nanoparticles supported on perovskite oxides are promising ones. However, little is known about their atomistic details, which are crucial for understanding and development of thermally stable catalysts. Herein, we present a machine-learning enhanced density functional theory study of Pd_xO_y nanoparticles supported on a $Sr_3Ti_2O_7$ (001) surface and demonstrate that supported oxidized Pd particles fulfill the conditions for the self-regenerative catalysts. In the oxidative condition, solid-solution reaction of Pd with the support is found to be preferable, but is limited to the vicinity of the surface. Furthermore, formation of PdO-like clusters enhances their binding strength to the support, inhibiting the agglomeration (sintering) of the $\mathrm{Pd}_x\mathrm{O}_y$ nanoparticles. We present detailed thermodynamic and electronic structure analyses and clarify the roles of the oxide support, cluster size of the oxidized metal nanoparticle, and the metal-support interaction. This work may provide a guideline for the rational design of the thermally stable catalyst against sintering.

Keywords: sintering; metal-support interaction; oxidative dispersion; global optimization; thermodynamics; machine learning; DFT.

Introduction

Thermal stability of heterogeneous catalysts, along with high activity and selectivity, plays a central role in the catalyst design for industrial applications,[1–4] e.g. three-way catalyst (TWC) converters to purify emission of exhaust gases[5–8] or fuel cells. However, the thermal instability originated from the agglomeration (sintering) of metal NPs over time under operating condition is the major concern, especially for the catalyst with metal NPs in small sizes.[9] Self-regenerable metal nanoparticles on the oxide surface show great potential to overcome this problem.[10–19] Metal oxide NPs are highly anchored on the oxide support under oxidative conditions with strong metal-support interaction (MSI) leading to the sintering resistance, while they are subsequently reduced back to active metallic NPs under reductive conditions.[10–19] This approach is often employed to prepare the ultrastable TWCs in which the platinum-group metal (PGM) NPs are exposed to the high-temperature reduction-oxidation (redox) fluctuations of exhaust gas.[10,20] PGM-O-M bonds (M is the metal of the support surface) formed in oxidative atmospheres can suppress sintering effectively.[12,18,21–29]

However, a very strong PGM-O-M bonding can lead to another deactivation process, i.e., a solid-solution reaction (SSR) under oxidative condition,[10–15] where the PGM ions are incorporated into the metal sites of oxide support. If the PGM cannot be reduced back to metallic NPs even under reductive conditions, the catalyst is deactivated.[12–15] For example, strong Rh-O-Al bonds in Rh/γ-Al_2O_3 effectively inhibit the sintering,[12,13,15] but the SSR between Rh_2O_3 and γ-Al_2O_3 deactivates the catalyst under the TWC oxidative condition. Replacing γ-Al_2O_3 with $LaMgAl_{11}O_{19}$ can help mitigate SSR because the La-O layer of $LaMgAl_{11}O_{19}$[12,13,15] suppresses the penetration of Rh^{3+} and preserves Rh^{3+} near the surfaces. Consequently, it is important to inhibit the direct PGM ions penetration from the support surface to the bulk region and to allow a smooth redox cycle of PGM NPs by TWC atmospheric fluctuation.[12–17]

Among the numerous candidates for the TWC support materials, titanate perovskite ($A\mathrm{TiO}_3$) and the related materials have received considerable research attention because of their chemical stability, strong anchoring effect, and low SSR.[14,16,17,25] Irvine *et al.* found that highly anchored Pt NPs on an A-site-deficient $A\mathrm{TiO}_3$ exhibits better catalytic NO + CO reaction activity and superior thermal stability.[14] Pt is incorporated into $A\mathrm{TiO}_3$ in the synthesis process and stable Pt clusters are formed upon reductive condition. During the reaction condition, self-regenerable Pt NPs are observed with a low SSR of Pt. Beppu *et al.* found that Ti-rich $\mathrm{SrFe}_x\mathrm{Ti}_{1-x}\mathrm{O}_{3-\delta}$-supported Pd catalysts (x = 0.0 and 0.2) have high catalytic activities for NO reduction and thermal stabilities under the stoichiometric condition because of the anchoring effect.[25] The catalysts was prepared by an impregnation method and PdO NPs are stable under the stoichiometric condition. However, the deactivation of $\mathrm{SrFe}_x\mathrm{Ti}_{1-x}\mathrm{O}_{3-\delta}$-supported Pd catalysts occurs under oxidative conditions. Very recently, well-dispersed and closely integrated Pd NPs supported on $Sr_3Ti_2O_7$ (STO-327) in a Ruddlesden–Popper phase have been synthesized. Here, the $Sr_3Ti_2O_7$-supported Pd catalyst shows the superior NO catalytic activity and thermal stability even after a long air-aging period.[30] Pd oxide (PdO) NPs with an average size of 2–5 nm are grown epitaxially on STO-327(001) surfaces with a strong metal-support interaction (MSI). The SSR of Pd with the STO-327 lattice is limited to the vicinity of the surface, presumably because of the presence of the rock-salt-type SrO layer that inhibits the diffusion of Pd atoms into bulk STO-327. However, the atomistic details of Pd (PdO) NPs, STO-327(001) surfaces, and their interfaces under operating conditions, which are crucial for the development of sintering-resistant catalysts, are yet to be elucidated.

Herein, we use density functional theory (DFT), machine learning enhanced global optimization, and thermodynamics to investigate the structures, oxidation states, and binding strengths of small Pd clusters (Pd_xO_y) supported on STO-327(001) under those relevant to the TWC conditions. We demonstrate that supported Pd_xO_y on STO-327 can be a self-regenerable catalyst with low SSR and strong MSI. First, we evaluate the possibility of the SSR of Pd and discuss the use of STO-327(001) to suppress SSR by constructing phase diagrams of Pd-doped bulk STO-327 and STO-327 surfaces. Next, we consider MSI by investigating the structures and binding strengths of several Pd_xO_y clusters on STO-327(001) and on non-hydroxyl-terminated γ-Al_2O_3(100). The PdO-like clusters supported on all surfaces are stabilized compared to the metallic Pd clusters, suggesting that the oxidative treatment can suppress the sintering and facilitate the metal redispersion effectively. Moreover, we find that Pd_xO_y clusters are more stabilized on STO compared with γ-Al_2O_3(100); and the origin for the stronger MSI at the Pd_xO_y/STO interface arises from charge-transfer interaction. The change in the atomic structure and stoichiometry of Pd clusters supported on STO surfaces under oxidative and reductive conditions is evaluated. Finally, we discuss the nucleation of PdO-like clusters under the oxidative condition: some clusters show peculiar stability against Ostward ripening. Strong interfacial bonding for these magic number clusters can explain the sintering resistance of Pd NPs supported on STO-327.

Methods

DFT+U calculations

All spin-polarized DFT calculations were performed using Quantum ESPRESSO package.[31] The PBEsol exchange-correlation functional[32] and ultrasoft pseudopotentials[33,34] were adopted. Wave functions and charge density were expanded by a plane wave basis set with kinetic energy cutoffs of 40 Ry and 320 Ry, respectively. The Hubbard U correction[35] with the effective U of 4.45 eV was employed for the Ti 3d states.[36] To mitigate the overbinding of the O_2 molecule, a correction of 1.11 eV was added to the total energy of O_2 (Figure S4).[37] Dispersion correction by Grimme[38,39] (PBEsol+U-D3) was used for the adsorption of (oxidized) Pd clusters on surfaces; whereas other calculations related to the bulk and surfaces of STO-327 were performed without dispersion correction (PBEsol+U). The Brillouin zone was sampled by the Monkhorst–Pack scheme[40] with a k-points distance of 0.20 Å^{-1}. The ionic relaxation was performed with a residual force threshold of 0.03 eV/Å (10^{-3} Ry/Bohr). The reaction path search was performed using the nudged elastic band (NEB) method.[41,42] Atomic charges were obtained using Löwdin population analysis.[43]

The crystal structures of STO-327 (Figure 1(a)) and $SrTiO_3$ (STO-113) considered herein have space groups of I4/mmm and P$\overline{m}$3m, respectively, where both STO-327 and STO-113 are assumed to retain their perovskite structures.[14,25] For comparison, we employed γ-Al_2O_3 using a nonspinel model and its nonhydroxyl terminated (100) surface.[44] The optimized lattice constants of STO-327, STO-113, and γ-Al_2O_3 are listed in the Supporting Information (SI).

Thermodynamics analysis

The formation of the Pd solid solution into the STO-327 bulk was evaluated by examining the stability of several Pd-doped STO-327 crystals (Pd@STO-327) in a $(2 \times 2 \times 1)$ supercell using the grand potential, which is defined as

$$\Omega_{\text{bulk}}(T, p_i) = G - \sum_i N_i \mu_i(T, p_i), \tag{1}$$

where G, $\mu_i(T, p_i)$, and N_i are the Gibbs free energy of Pd@STO-327, chemical potential of the atomic species i (i = Sr, Ti, O, Pd) at temperature T and partial pressure p_i, and number of atoms, respectively. All neutral atomic vacancies (V_{Sr}, V_{Ti}, V_{O}) and complex vacancies (V_{SrO}, V_{TiO}, V_{TiO_2}, and V_{SrTiO_3}) were considered for STO-327. For Pd@STO-327, we considered the substitution of Pd for the cations (Pd@Sr and Pd@Ti) and the substitution of Pd for the atom in the associated complex vacancies (Pd@C-V_V where C = Sr and Ti; V = Sr,Ti, and O).

The relative stability of STO-327 surfaces under conditions relevant to the TWC operating ones was investigated by calculating the surface excess free energy ($\Omega_{\mathrm{surf}}(T, p_i)$) and details are given in section SI.4 of SI.

We assumed that the structure is in equilibrium with bulk STO-327, which implies

$$3\mu_{\mathrm{Sr}} + 2\mu_{\mathrm{Ti}} + 7\mu_{\mathrm{O}} = \gamma^{\mathrm{bulk}}_{\mathrm{Sr_3Ti_2O_7}}, \tag{2}$$

where $\gamma^{\mathrm{bulk}}_{\mathrm{Sr_3Ti_2O_7}}$ denotes the Gibbs free energy of the bulk STO-327 per formula unit.

Vibrational frequencies and entropy were calculated within the harmonic approximation using Phonopy package.[45] Phonon contributions to the grand potential were found to be small with the order of 0.2 eV for $T < 1200$ K, which is in line with previous works.[46,47] As a result, thermodynamic stabilities of Pd@STO-327 and surface termination were evaluated without the phonon contribution. Then, we constructed phase diagrams of Pd@STO-327 and the STO-327 surfaces as a function of the chemical potentials of Sr ($\Delta\mu_{\mathrm{Sr}}$) and O ($\Delta\mu_{\mathrm{O}}$) relative to those of bulk Sr in the face-centered cubic (fcc) structure and gas-phase O_2, respectively. The ranges of $\Delta\mu_{\mathrm{Sr}}$ and $\Delta\mu_{\mathrm{O}}$ were restricted by the thermodynamical preference to form bulk STO-327 without the precipitation of constituent compounds,[48] namely SrO, TiO_2, Ti, Sr, and O_2 (See section SI.5 of SI). For the Pd chemical potential, we used bulk fcc Pd and tetragonal PdO as references, where $\mu_{\mathrm{Pd}} = E(\mathrm{Pd})$ if $\Delta\mu_{\mathrm{O}} \leq \Delta H_f(\mathrm{PdO})$, and $\mu_{\mathrm{Pd}} = E(\mathrm{PdO}) - \mu_{\mathrm{O}}$ otherwise. Here, $E(\mathrm{Pd})$, $E(\mathrm{PdO})$, and $\Delta H_f(\mathrm{PdO})$ are the total energies per formula unit of bulk fcc-Pd, tetragonal PdO, and enthalpy of formation of PdO, respectively.

Considering the system is in equilibrium with the O_2 atmosphere,[46,49] $\Delta\mu_{\mathrm{O}}$ can be estimated by

$$\begin{aligned}\Delta\mu_{\mathrm{O}}(T,p) &= \frac{1}{2}[\mu_{\mathrm{O}_2}(T,p) - E(\mathrm{O}_2)] \\ &= \frac{1}{2}[H_{\mathrm{O}_2}(T,p^0) - H_{\mathrm{O}_2}(0\ \mathrm{K},p^0)] \\ &- \frac{1}{2}T[S_{\mathrm{O}_2}(T,p^0) - S_{\mathrm{O}_2}(0\ \mathrm{K},p^0)] + \frac{1}{2}k_B T \ln\frac{p}{p^0},\end{aligned} \tag{3}$$

where $\mu_{\mathrm{O}_2}(T,p)$ is the O_2 chemical potential at temperature T and partial pressure p, $E(\mathrm{O}_2)$ is the DFT total energy of an isolated O_2, H is the enthalpy, S is the entropy, and p^0 is 1 atm. $H_{\mathrm{O}_2}(T,p^0)$ and $S_{\mathrm{O}_2}(T,p^0)$ are obtained from the NIST-JANAF thermochemical tables.[50]

In TWC, the reaction environment is changed frequently by sequential switching between fuel-lean and fuel-rich conditions, and this results in the change in the O_2 partial pressure (p_{O_2}). Moreover, thermal stability of TWC was tested by an air-aging experiment. The corresponding $\Delta\mu_{\mathrm{O}}$ for fuel-rich, stoichiometric, fuel-lean, and air-aiging conditions are tabulated in Table 1.[51,52]

Table 1: Relative chemical potential of an oxygen atom ($\Delta\mu_{\mathrm{O}}$) calculated using thermodynamics for the fuel-rich, stoichiometric, fuel-lean, and air-aging conditions. For the TWC operating conditions, the excess oxygen ratio (λ) and air-to-fuel weight ratio (A/F) are shown.[51,52] λ is defined as the amount of oxygen atoms in a gas feed divided by the amount of oxygen atoms under stoichiometric conditions.

Conditions	λ	A/F	T (K)	p_{O_2} (atm)	$\Delta\mu_{\mathrm{O}}$ (eV)
Fuel-rich	0.45	14.20	800	10^{-30}	-3.22
Stoichiometric	1.00	14.60	800	$10^{-11.3}$	-1.74
Fuel-lean	1.97	15.00	800	10^{-3}	-1.08
Air-aging			1200	0.20	-1.42

Global optimization of small supported $\mathrm{Pd}_x\mathrm{O}_y$

The structures of $\mathrm{Pd}_x\mathrm{O}_y$ clusters supported on STO surfaces were investigated using the global optimization with first-principles energy expression (GOFEE) algorithm,[53–55] which is based on the evolutionary algorithm and Gaussian process regression. The GOFEE method has been successfully applied for finding stable structures of supported metal clusters,[56,57] ultrathin oxide overlayer,[55] and aromatic hydrocarbons supported on graphene.[58] DFT calculations within GOFEE were performed using the grid-based projector augmented wave code[59] with the Perdew–Burke–Ernzerhof (PBE) functional,[60] double zeta-polarized basis, and a grid spacing of ≈ 0.20 Å. Only the Γ point was sampled. During global optimization, only atomic configurations of Pd_xO_y were optimized on a thin two-layer 1-unit-cell-thick STO-113 slab. To ensure the reliability, ten parallel GOFEE searches were performed and we considered the search is successful if a similar global minimum (GM) with a small distortion were found in 30% of the total GOFEE runs. Then, we reoptimized all non-equivalent structures within a 0.50 eV window from the set of the stable structures found by GOFEE using PBEsol+U-D3. The accuracy of this approach is discussed in SI SI.7. This approach is also applied to find stable Pt_xO_y on Ce(111)[56] and metal-embedded graphene.[57]

The binding strength of the supported Pd_xO_y clusters, i.e., the formation energy with respect to bulk fcc-Pd and tetragonal PdO, is calculated as

$$E_{\mathrm{f}}(\mathrm{Pd}_x\mathrm{O}_y) = \frac{1}{x}[E(\mathrm{Pd}_x\mathrm{O}_y/\mathrm{S}) - E(\mathrm{S}) - y \times E(\mathrm{PdO}) - (x - y) \times E(\mathrm{Pd})], \tag{4}$$

where $E(\mathrm{Pd}_x\mathrm{O}_y/\mathrm{S})$, $E(\mathrm{S})$, $E(\mathrm{PdO})$, and $E(\mathrm{Pd})$ are the total energies of the supported Pd_xO_y, clean surface, bulk tetragonal PdO, and bulk fcc-Pd per formula unit, respectively. A lower E_{f} indicates that Pd_xO_y is more stable on the support surface.

To investigate the composition of the supported Pd_xO_y clusters, we calculated the free energy of formation as

$$\Delta G_{\mathrm{f}}(\mathrm{Pd}_x\mathrm{O}_y) = G(\mathrm{Pd}_x\mathrm{O}_y/\mathrm{S}) - G(\mathrm{STO}) - x \times \mu_{\mathrm{Pd}} - (y - N_{\mathrm{V_O}}) \times \mu_{\mathrm{O}}(T, p), \tag{5}$$

where $G(\mathrm{Pd}_x\mathrm{O}_y/\mathrm{S})$, $G(\mathrm{STO})$, and $N_{\mathrm{V_O}}$ are the Gibbs free energies of Pd_xO_y/STO, pristine STO, and the number of oxygen vacancies (V_O's), respectively. The vibrational contribution of Pd_xO_y to $\Delta G_{\mathrm{f}}(\mathrm{Pd}_x\mathrm{O}_y)$ was not considered because it plays a minor role[61].

The effective charge q of supported Pd_xO_y is defined as $q = Z - q_{\mathrm{L}}$, where Z is the sum of the valencies of constituent atoms and q_{L} is the sum of the number of valence electrons estimated by the Löwdin population analysis.

Results and Discussion

Solid solution reaction of Pd with STO-327

The Pd solid solution is studied by elucidating the stability of Pd@STO-327 in equilibrium with gas-phase O_2. The kinetic of the Pd dissolution is beyond the scope of the present study and we encourage others to employ molecular dynamics or NEB methods to explore this problem.[62,63] The crystal structure of STO-327 with five different surface terminations of the (001) facet is shown in Figure 1 (a). The stable phases in the $(\Delta\mu_{\mathrm{O}}, \Delta\mu_{\mathrm{Sr}})$ space are shown in Figure 1 (b), and the crystal structures of Pd@STO-327 are shown in Figure S6. The hatched region represents the stable region of bulk STO-327 without the precipitation of the associated compounds (SrO, TiO_2, Ti, Sr, and O_2) and typical TWC operating conditions are located in a region limited by two white dotted lines, i.e -3.22 eV $< \Delta\mu_{\mathrm{O}} < -1.08$ eV. As shown in Figure 1 (b), pristine STO-327 is the most stable phase under the reductive conditions ($\Delta\mu_{\mathrm{O}} <$ ca. -1.8 eV); while the Pd solid solution is preferably formed, where the Pd atoms occupy the Ti sites (Pd@Ti, 3Pd@Ti, and 4Pd@Ti) without any defects, under the oxidative conditions ($\Delta\mu_{\mathrm{O}} >$ ca. -1.8 eV). We found that the PdO_6 octahedra is distorted and tilted from the ideal TiO_6 octahedra because of the strain effect of the STO-327 lattice (Figure S6). The Pd@Ti structure with the a distorted PdO_6 octahedron is more stable than that with an undistorted PdO_6 octahedron by 14 meV. On the other hand, the 4Pd@Ti structure with the distorted PdO_6 octahedra in the PdO_2 layer is more stable than that with the undistorted PdO_6 octahedra by 0.55 eV, showing that the distortion of PdO_6 plays a more crucial role in the high Pd doping concentration. We find that the planar PdO_4 coordination that formed in bulk PdO cannot be formed in Pd@STO-327. To form a PdO_4 configuration in bulk STO-327, two V_{O} formations are required. In the case of Pd@Ti, this occurs under a rather reductive condition, i.e. $\Delta\mu_{\mathrm{O}} < -7.1$ eV, showing that planar PdO_4 coordination

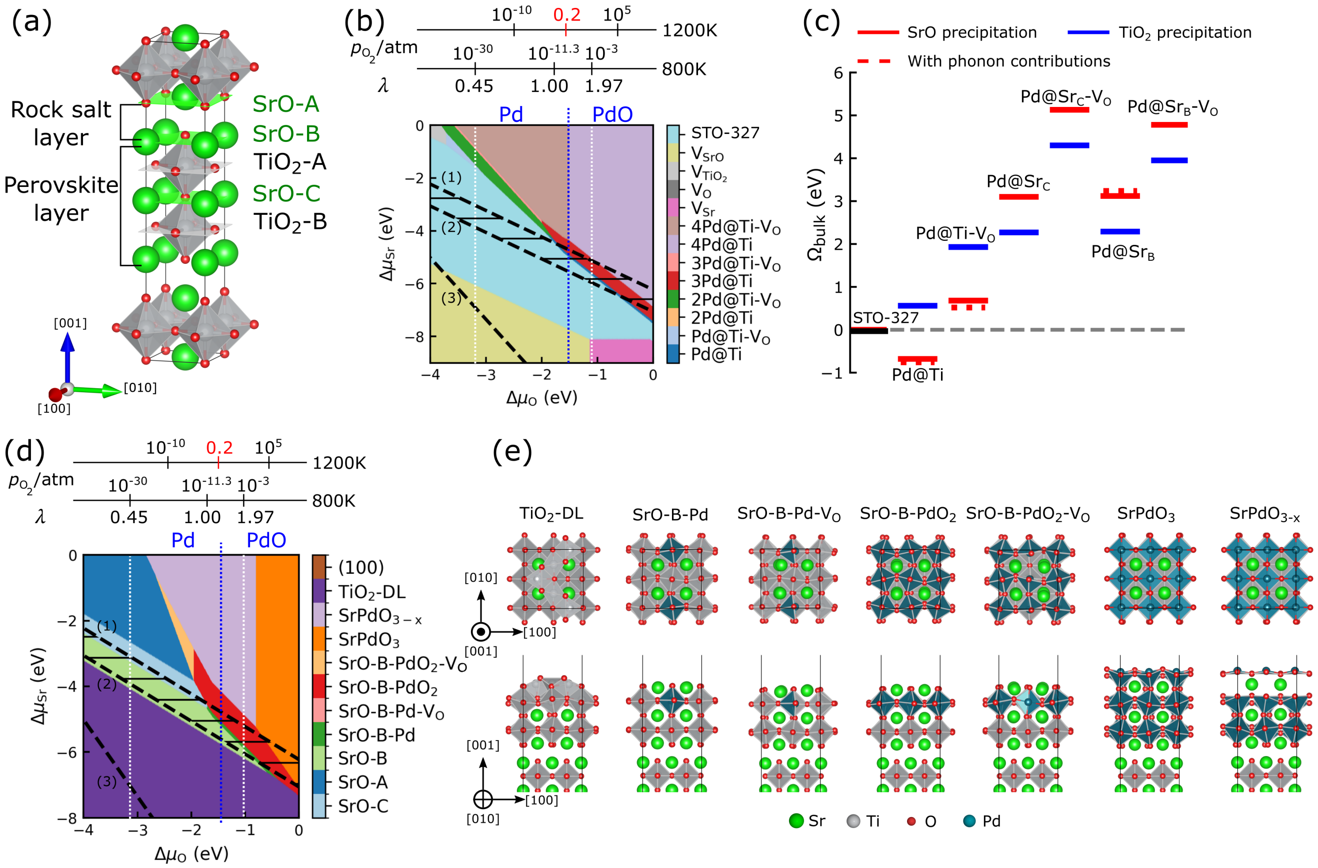

Figure 1: (a) Crystal structure of STO-327 with various terminating (001) planes. (b) Phase diagram of STO-327 with several defects and Pd@STO-327 in the $(\Delta\mu_{\mathrm{O}}, \Delta\mu_{\mathrm{Sr}})$ space. (c) Grand potentials of a single Pd substituted for Ti (Pd@Ti) and for Sr at the perovskite (Pd@$\mathrm{Sr_C}$) and rock-salt (Pd@$\mathrm{Sr_B}$) layers under the fuel-lean condition. The grand potentials at the SrO and $\mathrm{TiO_2}$ precipitation boundaries are shown in red and blue, respectively. The phonon contributions to grand potentials of Pd@Ti, Pd@Ti-$\mathrm{V_O}$, and Pd@Sr are elucidated. (d) Phase diagrams of the (001) and (100) surfaces of STO-327 in the $(\Delta\mu_{\mathrm{O}}, \Delta\mu_{\mathrm{Sr}})$ space and (e) atomic models of STO-327(001). For the phase diagrams, the hatched region corresponds to the region where STO-327 is thermodynamically stable without the deposition of associated compounds, which is defined by (1) SrO, (2) $\mathrm{TiO_2}$, (3) Ti, and $\mathrm{O_2}$ ($\Delta\mu_{\mathrm{O}} \leq 0$) precipitation lines. The area between two white dotted lines corresponds to typical $\mathrm{O_2}$ conditions in TWC. The blue line represents the bulk PdO/Pd thermodynamic phase equilibrium at $\Delta\mu_{\mathrm{O}} = -1.59$ eV.

is hardly formed in Pd@STO-327. When the environment is changed from the TiO_2-rich condition [the region near line (2)] to the SrO- rich [the region near line (1)] condition, the Pd solid-solution becomes favorable at a lower $\Delta\mu_{\mathrm{O}}$ (-0.8 eV to -1.7 eV), indicating that the SSR of Pd proceeds more easily under the SrO-rich conditions. Consequently, the Pd solid solution is thermodynamically preferable under oxidative SrO-rich conditions, where Pd is incorporated into the Ti site. The appearance of SSR highlights the strong MSI of Pd NPs with STO-327.

The above analysis indicates that Pd can be dissolved into the STO-327 bulk region in oxidative conditions, confirming that SSR is highly probable and may cause catalyst degradation. However, we discuss that the SrO rock-salt layer of STO-327 plays an important role to inhibit the Pd penetration deep into the STO-327 bulk region. To this end, we compare the stability of Pd substituted for the Ti (Pd@Ti) and Sr sites (Pd@$\mathrm{Sr_C}$ and Pd@$\mathrm{Sr_B}$) under the fuel-lean condition ($\Delta\mu_{\mathrm{O}} = -1.08$ eV). In Figure 1 (c), the stability of the substituted Pd at the SrO precipitation [line (1)] and TiO_2 precipitation [line (2)] boundaries are shown by red and blue lines, respectively. Under the SrO-rich condition, Pd@Ti is preferable, whereas Pd@Sr's are significantly less stable than Pd@Ti by at least 3.78 eV. To diffuse along the [001] direction, Pd should cross the SrO rock-salt layer; however, to cross the SrO rock-salt layer, Pd must be substituted for Sr. Therefore, thermodynamic barrier for the Pd dissolution from STO-327(001) to the bulk region is approximately the grand potential difference between Pd@Ti and Pd@Sr. The instability of Pd substitution for the Sr site suggests that the diffusion of Pd is suppressed along the [001] direction. Under the TiO_2-rich condition, Pd@Sr structures are stabilized compared with that under the SrO-rich condition. However, Pd@Sr's are less stable than Pd@Ti by at least 1.37 eV. Furthermore, the Pd dissolution becomes less stable than pristine STO-327. Hence, under both SrO-rich and TiO_2-rich conditions, the Pd diffusion along the [001] direction should be suppressed by the SrO rock-salt layer, which is parallel to the STO-327(001) surface. Thus, the Pd penetration from the STO-327(001), which is found to be the most stable (Figure 1 (d)), to the bulk region is mitigated. Consequently, the SSR between Pd and STO-327 is rather limited near the subsurface,[13] suggesting that STO-327(001) can suppress the undesired SSR in the oxidative atmosphere.

We here discuss the phonon contributions to the grand potential of Pd@STO-327. Details on the phonon analysis and free energy estimation are in section SII of SI. The Ω_{bulk}'s of Pd@Ti, Pd@Ti-V_O, and Pd@Sr_B remain almost unchanged regardless of the phonon contribution under TWC oxidative condition at $T = 800$K and the SrO precipitation condition (Figure 1 (c)). The phonon contribution plays a minor role in the thermodynamic stability of Pd@STO-327 (Figure S8), and thus our conclusions regarding Pd solid solution and the role of the SrO layer are not altered.

The stable phases of the STO-327(001) and (100) surfaces in the $(\Delta\mu_{\mathrm{O}}, \Delta\mu_{\mathrm{Sr}})$ space are shown in Figure 1 (d), and the corresponding atomic structures are depicted in Figure 1 (e). The SrO-terminated (001) surface generated by cleaving at the rock-salt layer (SrO-B)[64] is stable under reductive conditions, whereas SrO-C is formed preferably only at $\Delta\mu_{\mathrm{O}} \leq -1.8$ eV under the SrO-rich condition. Under oxidative SrO-rich conditions ($-1.8 < \Delta\mu_{\mathrm{O}} < -1.0$ eV), Ti of the subsurface TiO_2 layer is substituted with Pd (SrO-B-Pd and SrO-B-PdO_2), whereas under the TiO_2-rich condition, the stable surface is SrO-B. The surface stabilities of STO-327(001) and (100) at the SrO and TiO_2 precipitation lines are shown in Figure S9.

Metal-support interaction of the supported Pd_xO_y

Enhanced bonding by the cluster oxidation

To elucidate the MSI of supported Pd clusters, we evaluate the binding strengths of several Pd_xO_y clusters to STO-327(001) and to γ-Al_2O_3(100). The most stable STO-327(001) surfaces are composed of simple $SrTiO_3$ pevroskite layers with a SrO termination. Therefore, we simplify our support models to study the MSI of the supported Pd_xO_y by using both SrO- and TiO_2- terminated STO-113(001) surfaces (SrO-STO-113 and TiO_2-STO-113). The detailed GOFEE sampling is given in SI.6.

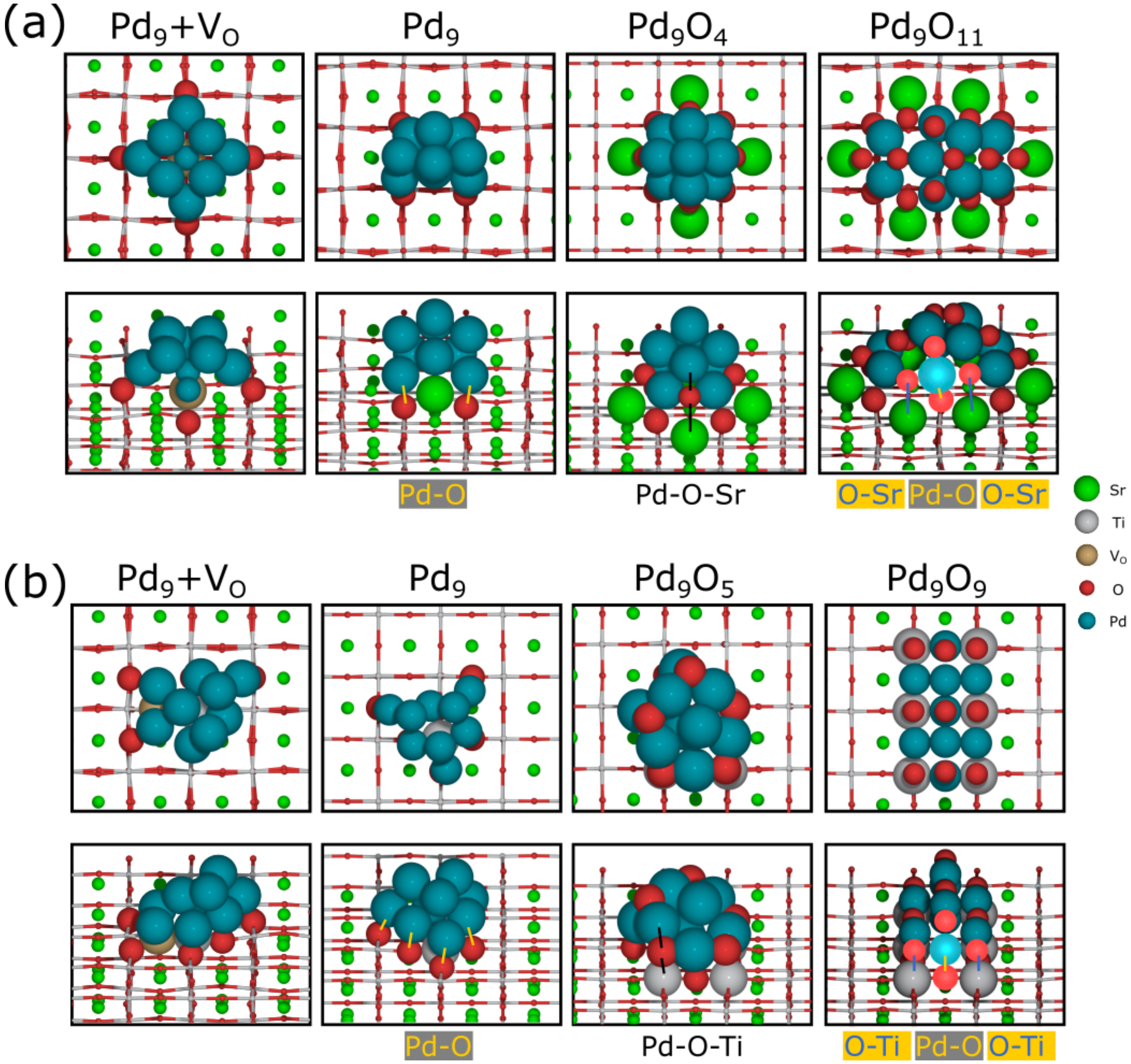

Figure 2: The atomic geometries of the stable Pd_9O_y supported on (a) SrO- and (b) TiO_2-STO-113. Large spheres represent the cluster and surface atoms involved in the interfacial bonds. The glowed spheres indicate O atoms involved in the anchoring PdO_4 bonding configuration at the interface.

We begin by discussing the structural change of the supported Pd cluster upon cluster oxidation. The atomic geometries of the stable Pd_9O_y clusters on SrO- and TiO_2-STO-113's are shown in Figures 2 (a) and (b), respectively, and those of Pd_9O_y on γ-$Al_2O_3(100)$ are shown in Figure S10. Furthermore, the atomic geometries of Pd_xO_y with different cluster sizes on three supports are depicted in Figures S11 − S15. On three supports, the structural transition of Pd_xO_y ($x > 4$) takes place from compact fcc-like shapes for the metallic clusters ($y = 0$) to almost planar structures for the PdO-like clusters ($y/x \geq 1$). Figure 2 shows that the supported metallic Pd_9 clusters have bulk fcc-Pd shapes and bind to the STO-113 surfaces via Pd- surface O bonds. In contrast, the PdO-like clusters have raft-like shapes and bind to the STO-113 surfaces via both Pd- surface O and cluster O - Sr/Ti bonds, which results in the shape transition. The interfacial bonds in PdO-like clusters create anchoring PdO_4 bonding configurations with the substrate, which is observed in CeO_2-supported Pd and Pt NPs.[27,65,66] For the supported Pd_xO_y in the low oxidation state ($y = x/2$ or $(x+1)/2$), most oxygen atoms occupy the perimeter sites of Pd clusters to create Pd-O-Sr/Ti bonds (Figure 2); some O atoms are adsorbed on Pd clusters at hollow sites. A similar structural transition of the Pd_xO_y clusters on γ-$Al_2O_3(100)$ upon cluster oxidation is observed.

Figure 3(a) shows the calculated E_f's of Pd_xO_y on SrO-, TiO_2-STO-113's and γ-Al_2O_3. Overall, E_f's decrease monotonically with increasing oxygen content up to $y/x \simeq 1$ and they increase above $y/x \geq 1$, implying that the MSI between Pd_xO_y and support is enhanced upon the oxidation of the cluster and the interaction of the PdO-like clusters with the support is the strongest. Therefore, the agglomeration of oxidized Pd clusters is mitigated in the oxidative atmospheres via the anchoring effect[21,24,67] and highly dispersed PdO NPs with a small size may be retained. Moreover, the cluster oxidation can regulate the catalytic activity[68] and the binding strength of adsorbate.[61]

In the experiments, the sintering resistance is significantly improved in the oxidative atmosphere, where PGM NPs are in the oxide state rather than in the reductive atmosphere, where PGM NPs are in the metallic state.[9,21,22,56,69–76] Nagai *et al.* found that the sintering

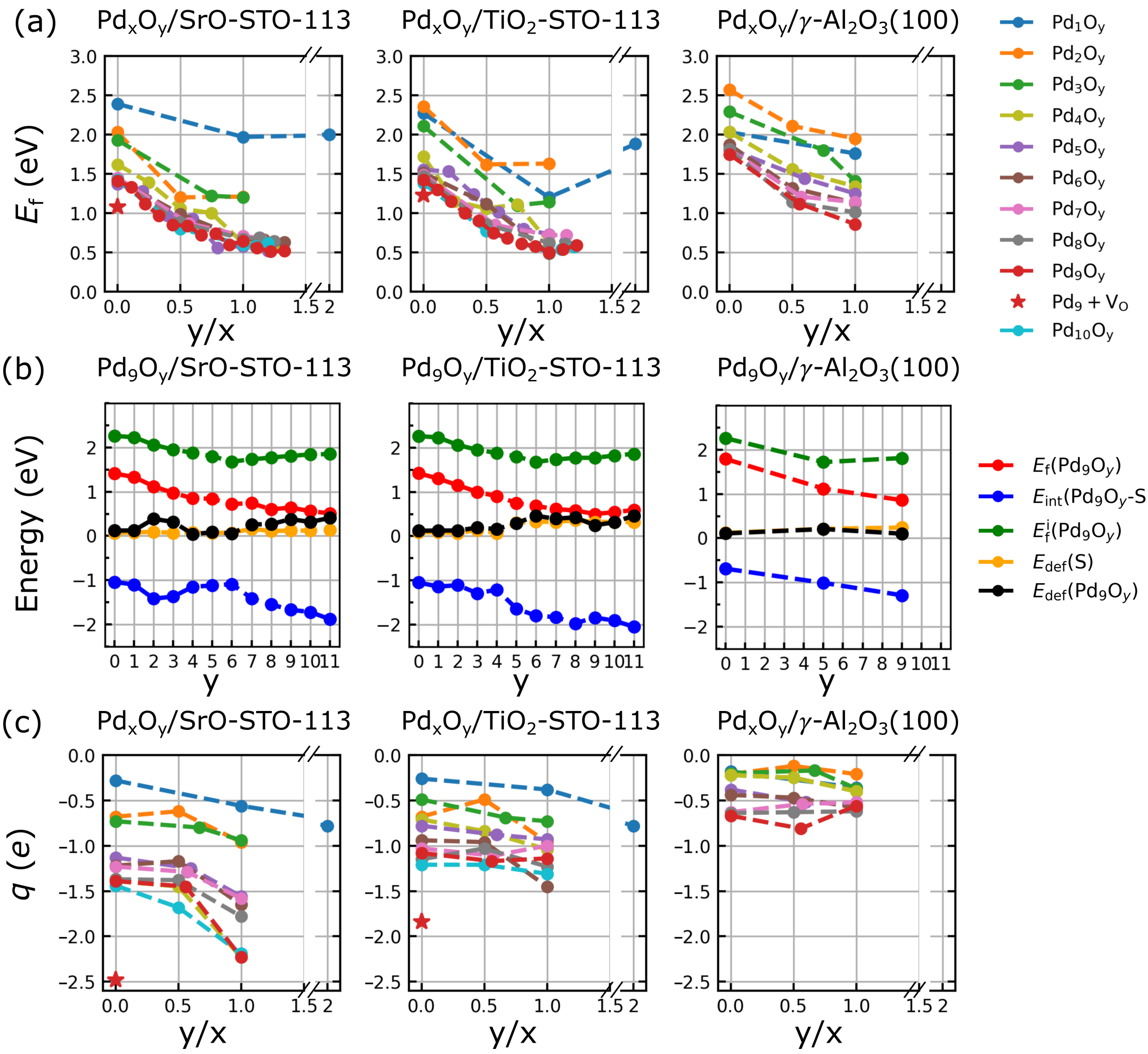

Figure 3: (a) Formation energy (E_f) of Pd_xO_y on SrO- and TiO_2-STO-113's and γ-Al_2O_3(100). (b) Energy decomposition analysis of Pd_9O_y supported on SrO-, TiO_2-STO-113's, and γ-Al_2O_3(100). (c) Effective charge (q) of supported Pd_xO_y. The figure legend is similar with that of (a).

inhibition of Pt NPs supported on CeO_2 under the air-aging condition originates from the formation of PtO_2 NPs, where Pt-O-Ce bonds stabilize PtO_2 NPs at $T = 1073$ K.[21,22] Cuenya *et al.*[70,72,73] found the enhanced stabilization of γ-Al_2O_3- and SnO_2- supported Pt NPs after oxidative pretreatment, which is supposedly attributed to the formation of PtO_x species with Pt-O interfacial bonds (or Pt-OH in H_2O pretreatment) at $T = 673$ K. Our results are in line with recent DFT reports on $Pt_{13}O_x$ on γ-Al_2O_3(100)[76] and Pt_6O_x on CeO_2(111).[56]

We note that metal NP often undergoes a partial oxidation with a thin metal oxide layer formation in the strong metal-support interaction.[77] The size of metal NPs has a strong influence in its oxidation state, in which the larger NP is more difficult to oxidize,[78] hence the partially oxidized state may be observed experimentally in the oxidative treatment. As will be shown later, in the small size regime (Pd_9O_y) considered herein, the full oxidized state is stable under normal oxidative conditions and the partially-oxidized state is stable under rather reductive condition.

The sintering resistance of STO-327 is further highlighted by comparing the binding strengths of Pd_xO_y supported on STO-113 with those on γ-Al_2O_3. Figure 3 (a) shows that the E_f's of Pd_xO_y on both SrO- and TiO_2-STO-113's are smaller than those on the γ-Al_2O_3 surface, indicating the stronger binding strength of Pd_xO_y clusters to the STO surfaces. The average E_f's of small metallic Pd_x clusters ($x \geq 4$) on SrO- and TiO_2-STO-113 are 1.45 and 1.52 eV, respectively, while that of γ-Al_2O_3 (100) is 1.85 eV. Moreover, the average E_f's of stoichiometric Pd_xO_x ($x \geq 4$) on SrO- and TiO_2-STO-113's (0.65 and 0.57 eV) are significantly smaller than that of γ-Al_2O_3 (100) (1.12 eV). These results highlight that the Pd_xO_y clusters are further stabilized on the STO support compared with those on γ-Al_2O_3.

Energy decomposition analysis and charge state of Pd_xO_y

Using Pd_9O_y as a representative cluster, the energy decomposition analysis is performed to provide insight into MSI of the supported Pd_xO_y and the increase in MSI upon cluster oxidation, as shown in Figure 3 (b). The formation energy of Pd_9O_y, $E_\mathrm{f}(Pd_9O_y)$, is decomposed into the cluster-substrate interaction energy $E_\mathrm{int}(Pd_9O_y\text{-S})$, isolated (intrinsic) cluster formation energy $E_{\mathrm{f}}^{\mathrm{i}}(\mathrm{Pd}_9\mathrm{O}_y)$, deformation energy of the cluster $E_{\mathrm{def}}(\mathrm{Pd}_9\mathrm{O}_y)$, and deformation energy of the substrate $E_{\mathrm{def}}(\mathrm{S})$ (SI SI.8). From Figure 3(b), we find that interactions between $\mathrm{Pd}_9\mathrm{O}_y$ and the substrates are greatly strengthened upon cluster oxidation as indicated by a decrease in $E_{\mathrm{int}}(\mathrm{Pd}_9\mathrm{O}_y\text{-S})$ from $y = 0$ to 11 by 0.9 eV. The intrinsic formation energy of the $\mathrm{Pd}_9\mathrm{O}_y$ cluster, as characterized by $E_{\mathrm{f}}^{\mathrm{i}}(\mathrm{Pd}_9\mathrm{O}_y)$, is moderately decreased from the fully reduced Pd_9 (2.26 eV) to $\mathrm{Pd}_9\mathrm{O}_6$ (1.68 eV); and it is then slightly increased to the PdO-like $\mathrm{Pd}_9\mathrm{O}_9$ cluster (1.77 eV). The energies required to deform the substrate ($E_{\mathrm{def}}(\mathrm{S})$) and isolated $\mathrm{Pd}_9\mathrm{O}_y$ clusters ($E_{\mathrm{def}}(\mathrm{Pd}_9\mathrm{O}_y)$) to their adsorbed geometries are moderately increased by 0.3 eV. As the result, the isolated cluster formation energy and deformation energies compensate each other and MSI of the supported cluster mainly governs by cluster-substrate interaction. Therefore, we conclude that the stronger MSI of the PdO-like clusters arises solely from the electronic interactions between PdO-like clusters and support surfaces.

The energy decomposition analysis in Figure 3 (b) also reveals that the stronger MSI of Pd/STO-327 than Pd/γ-$\mathrm{Al}_2\mathrm{O}_3$ mainly arises from electronic interactions between Pd NPs and substrate. The lower E_{f} of $\mathrm{Pd}_9\mathrm{O}_y$ on STO-113's compared with that on γ-$\mathrm{Al}_2\mathrm{O}_3$ originates from the interaction of $\mathrm{Pd}_9\mathrm{O}_y$ with the substrate. $E_{\mathrm{int}}(\mathrm{Pd}_x\mathrm{O}_y\text{-S})$ of Pd_9/SrO-STO-113 and Pd_9/TiO_2-STO-113 are -1.04 and -1.05 eV, respectively, which are considerably more stable than that of Pd_9/γ-$\mathrm{Al}_2\mathrm{O}_3$ (-0.69 eV).

The effective charges (q's) of the supported $\mathrm{Pd}_x\mathrm{O}_y$ clusters by the Löwdin population are shown in Figure 3 (c). All q's are negative, showing that CT takes place from the substrate to the $\mathrm{Pd}_x\mathrm{O}_y$ clusters in all cases, leading to the $\mathrm{Pd}_x\mathrm{O}_y$ clusters are negatively-charged upon adsorption.[79] We find that the magnitude of CT from the support surface to the $\mathrm{Pd}_x\mathrm{O}_y$ clusters are in order SrO-STO-113 > TiO_2-STO-113 > γ-$\mathrm{Al}_2\mathrm{O}_3$(100). On STO substrates, the PdO-like clusters at $y/x = 1$ are further negatively charged compared with the metallic clusters ($y = 0$). It indicates that CT plays an important role in the stronger MSI of the PdO-like cluster on the STO support.[80] In contrast, the CT magnitude and CT change upon cluster oxidation for $\mathrm{Pd}_x\mathrm{O}_y$/$\gamma$-$\mathrm{Al}_2\mathrm{O}_3$ (100) are considerably small.

Our results imply that a strong MSI of Pd NPs with the STO support via the electronic interactions, in which the CT interaction[81–83] plays a crucial role, inhibits the sintering of Pd NPs on STO as observed by Tanaka *et al.*[25] at T > 1100 K. In contrast, the MSI between Pd NPs and γ-Al_2O_3 is weak, and thus, γ-Al_2O_3-supported Pd NPs would sinter quickly at this temperature.

Electronic structure analysis

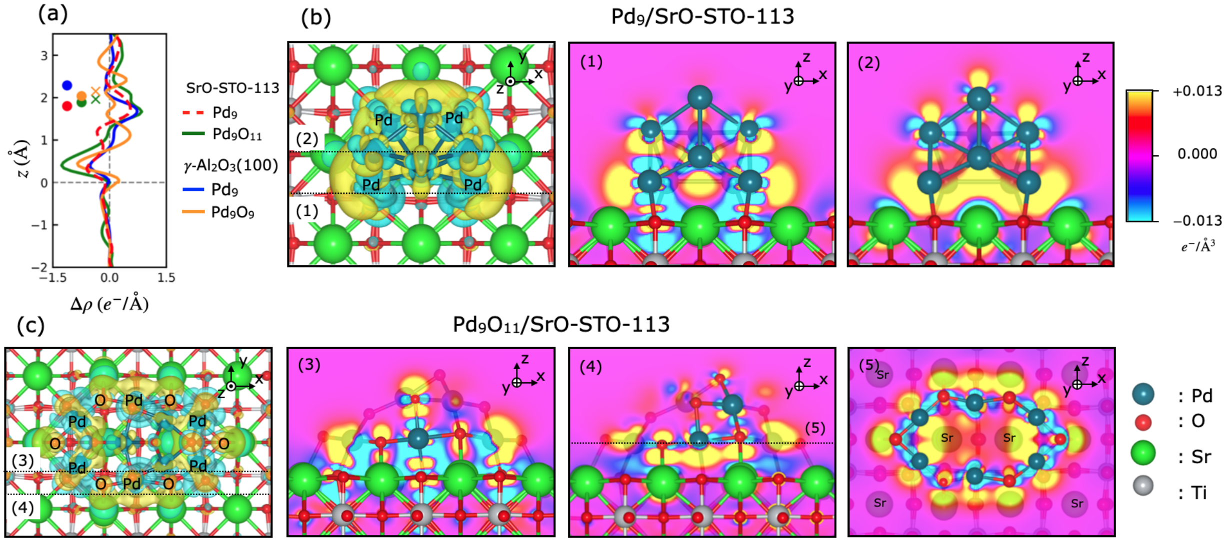

Figure 4: (a) Plane-averaged $\Delta\rho$ along the z direction of Pd_9 and Pd_9O_{11} on SrO-STO-113; Pd_9 and Pd_9O_9 on γ-Al_2O_3(100). Red, blue, green, and orange circle markers denote the average heights of the interfacial cluster Pd atoms in Pd_9/SrO-STO-113, Pd_9/γ-Al_2O_3(100), Pd_9O_{11}/SrO-STO-113, and Pd_9O_9/γ-Al_2O_3(100) respectively; while green and orange x markers denote the average heights of the interfacial O atoms in Pd_9O_{11}/SrO-STO-113 and Pd_9O_9/γ-Al_2O_3(100), respectively. The gray dashed line indicates the z position of the substrate topmost layer. Top views and projections of the calculated $\Delta\rho$'s onto the plane containing the interfacial bonds of (b) Pd_9/SrO-STO-113 and (c) Pd_9O_{11}/SrO-STO-113. Isosurfaces are plotted at 0.013 $e^-/\text{Å}^3$ with yellow and cyan color represent charge accumulation and charge depletion, respectively. The projections (2) and (5) indicate the electrostatic attractions driven by Pd 4d orbitals polarization in Pd_9 and Pd_9O_{11} on SrO-STO-113.

We first analyze the CT interaction between Pd_xO_y with oxide supports. We inspect the charge density difference ($\Delta\rho$) of Pd_xO_y on SrO-STO-113 and γ-Al_2O_3(100) to provide the

Table 2: Average change in Löwdin population (Δq_{L}) of the interface Pd $4d$, Pd $5sp$, and O $2p$ upon adsorption on the substrates. The unit is electrons (e^-). A negative value of Δq_{L} indicates the decrease in the electron population upon the adsorption of Pd_9O_y on the substrate and vice versa.

Structure	$4d_{3z^2-r^2}$	$4d_{x^2-y^2}$	$4d_{xz}$	$4d_{yz}$	$4d_{xy}$	e_g	t_{2g}	sp	O $2p$
Pd_9/SrO-STO-113	−0.12	0.07	−0.01	−0.11	0.01	−0.04	−0.10	0.39	
Pd_9O_{11}/SrO-STO-113	−0.18	0.01	0.02	0.00	0.12	−0.17	0.14	0.21	0.17
Pd_9/γ-Al_2O_3(100)	−0.03	0.04	−0.09	0.00	0.03	0.01	−0.06	0.18	
Pd_9O_9/γ-Al_2O_3(100)	−0.20	0.04	0.05	0.06	0.01	−0.16	0.11	0.14	0.11

insights into the CT mechanism. $\Delta\rho$ is defined as $\Delta\rho(\mathrm{Pd}_9/S) = \rho(\mathrm{Pd}_9/S) - \rho(\mathrm{Pd}_9) - \rho(S)$. The plane-averaged $\Delta\rho$ for Pd_9, Pd_9O_{11} on SrO-STO-113 and Pd_9, Pd_9O_9 on γ-Al_2O_3(100) along the z direction are shown in Figure 4 (a); while the $\Delta\rho$ maps for Pd_9 and Pd_9O_{11} on SrO-STO-113 are shown in Figure 4 (b) and (c), respectively. Average change in Löwdin population (Δq_{L}) of the interface Pd $4d$, Pd $5sp$, and O $2p$ upon adsorption on the substrates are tabulated in Table 2.

The plane-averaged $\Delta\rho$ along z direction in Figures 4 (a) and S22 show that the charge is accumulated beneath Pd clusters ($1.0 < z < 2.0$ Å), while the charge is depleted above the substrate topmost layer ($0.1 < z < 0.9$ Å) for both metallic and oxidized Pd_9O_y clusters on SrO-STO-113, TiO_2-STO-113, and γ-Al_2O_3(100). It confirms that the CT interactions occur from those substrates to Pd clusters as indicated by q in Figure 3 (c). The negatively-charged states of Pd_xO_y are consistent with previous reports on Pt/STO-113,[84] Au/STO-113,[85] Rh_2/γ-Al_2O_3(100),[80] and Pd_9O_y/γ-Al_2O_3(100).[79]

The energy positions relative to vacuum level (E_{vac}) of the conduction band minimum (CBM) and valence band maximum (VBM) of the support surfaces and that of the highest occupied molecular orbital (HOMO) and the lowest unoccupied molecular orbital (LUMO) of the Pd_9O_y are crucial for the CT interaction. Those energy positions for clean substrates, i.e. SrO-STO-113, TiO_2-STO-113, and γ-Al_2O_3(100) and isolated Pd_9O_y are shown in Figure 5 (a). The VBM and CBM of the deformed substrate and HOMO and LUMO of the deformed Pd_9O_y (denoted with superscript ^{a}), where atomic geometries are fixed at their adsorption

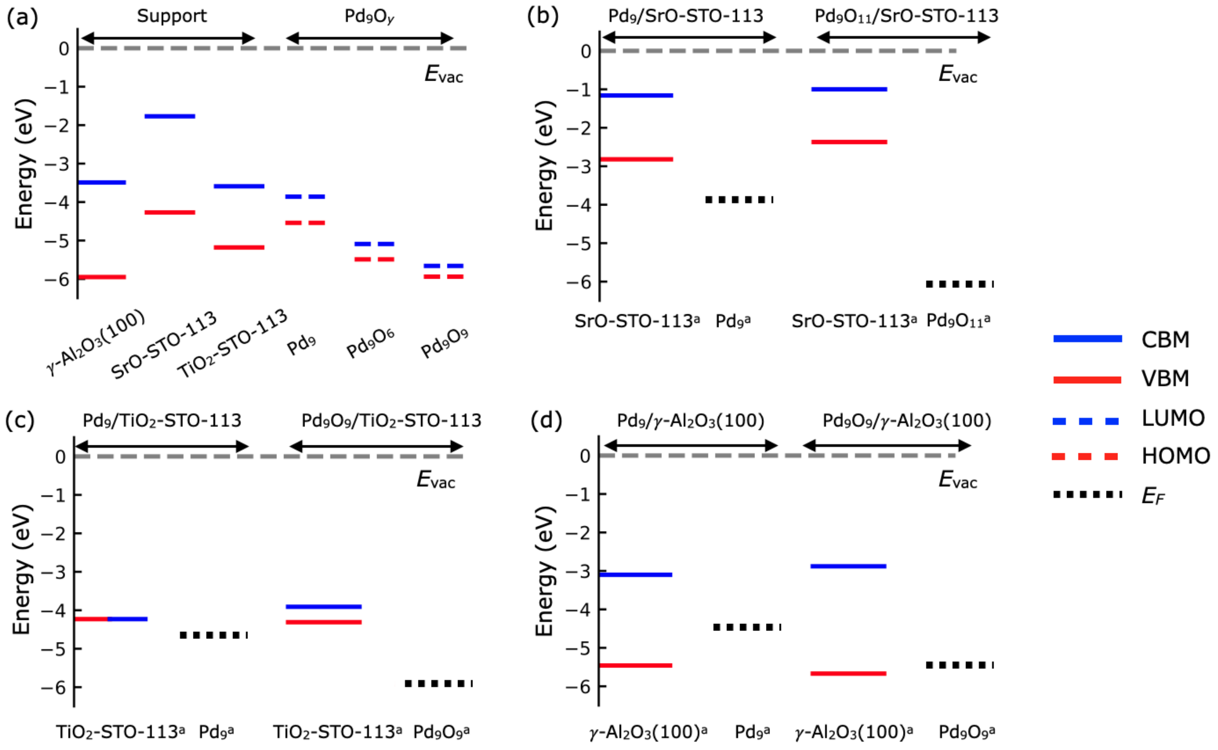

Figure 5: (a)Energy positions of the conduction band minimum (CBM) and valence band maximum (VBM) of the clean support surfaces, i.e. SrO-STO-113, TiO$_2$-STO-113, and γ-Al$_2$O$_3$(100); and energy position of the highest occupied molecular orbital (HOMO) and the lowest unoccupied molecular orbital (LUMO) of the isolated Pd$_9$O$_y$ (y = 0, 6 and 9). E_{vac} is the vacuum level, which is defined as the average electrostatic potential at the center of the vacuum region. Energy positions of CBM and VBM of the deformed substrate; HOMO and LUMO of the deformed Pd$_x$O$_y$ for (b) Pd$_9$ and Pd$_9$O$_{11}$ on SrO-STO-113, (c) Pd$_9$ and Pd$_9$O$_9$ on TiO$_2$-STO-113, and (d) Pd$_9$ and Pd$_9$O$_9$ on γ-Al$_2$O$_3$(100). The deformed substrate (S$^{\text{a}}$) and cluster (Pd$_9$O$_{\text{y}}$$^{\text{a}}$) have geometries fixed at Pd$_9$O$_y$/S.

geometries, for Pd_9O_y on SrO-STO-113, TiO_2-STO-113, and γ-$Al_2O_3(100)$ are shown in Figure 5 (b), (c), and (d), respectively. From Figure 5 (a), the energy of VBM, which plays a role of the donor orbital, of clean SrO-STO-113, TiO_2-STO-113, and γ-$Al_2O_3(100)$, are -4.27, -5.18, and -5.95 eV, respectively; showing that both STO-113's are better electron-injection substrates than γ-$Al_2O_3(100)$. Moreover, the VBM positions of three clean supports generally explain the CT order in Figure 3 (c), where the magnitudes of $q(Pd_xO_y)$ are in order SrO-STO-113 $>$ TiO_2-STO-113 $>$ γ-$Al_2O_3(100)$.

Cluster oxidation lowers the energy levels of Pd_xO_y LUMO, which plays a role of acceptor orbital, in both isolated and deformed geometries (Figure 5), thus the electron injection from the substrates to Pd_xO_y is more preferable upon cluster oxidation. This decrease in the LUMO level generally explains the increase in CT interaction and MSI upon cluster oxidation for Pd_xO_y supported on SrO- and TiO_2-STO-113 substrates as indicated by Figure 3 (b) and (c).

We then inspect the energy levels of deformed substrates and clusters in Figures 5 (b-d). The deformed Pd_xO_y's become metallic in all cases. The Fermi levels (E_F) of Pd_xO_y are lower than SrO- and TiO_2-STO-113 VBM's, indicating that interunit CT interactions from STO-327 to Pd_xO_y occur easily. On the other hand, for Pd_9/γ-$Al_2O_3(100)$, E_F of $Pd_9{}^a$ is -4.49 eV, while the VBM and CBM of γ-$Al_2O_3(100)^a$ are -5.46 and -3.10 eV, respectively (Figure 5 (d)). The pushback effect, in which charge flows from more contracted orbitals of closed shell system (γ-$Al_2O_3(100)$) to more diffuse orbitals of open shell system (Pd_9), is crucial to enable the CT from γ-$Al_2O_3(100)$ to metallic Pd cluster.[86] The cluster oxidation brings E_F of $Pd_9O_9{}^a$ to -5.47 eV, but it is still slightly higher than VBM of γ-$Al_2O_3(100)^a$ (-5.67 eV). The VBM at a rather low energy relative to the vacuum level of γ-$Al_2O_3(100)$ hinders the charge exchange with Pd_xO_y, leading to weaker MSI of Pd_xO_y on γ-Al_2O_3.

Having analyzed the CT interaction, we now reveal the binding mechanism of the Pd clusters to SrO-STO-113. The interactions between Pd_9 and SrO-STO-113 are governed by inter-unit CT and further stabilized by intra-unit polarization. The $\Delta\rho$ map in Figure 4 (b)

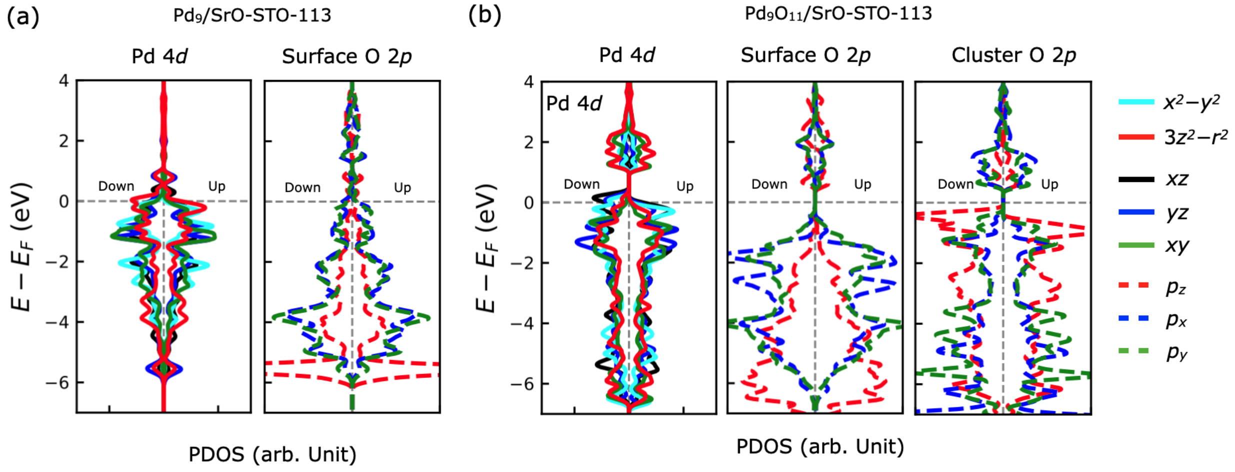

Figure 6: (a) Projected density of states (PDOS) onto the interfacial cluster Pd 4*d* states and surface O 2*p* states in the first layer of the substrate of Pd_9/SrO-STO-113. (b) PDOS onto interfacial cluster Pd 4*d*, surface O 2*p* states in the first layer of the substrate, and interfacial cluster O 2*p* states of Pd_9O_{11}/SrO-STO-113.

reveals that the charge depletion locates along the z direction of the interfacial Pd atoms, while the charge accumulation locates in the xy plane of the interfacial Pd atoms toward Sr sites. It indicates the electrons of Pd atoms are polarized by the interactions with support. Table 2 shows that interfacial Pd 5*sp* orbitals are further populated, while Pd 4*d* orbital are less populated upon adsorption on SrO-STO-113. The projected density of state (PDOS) of the interfacial cluster Pd 4*d* and surface O 2*p* in the first layer of SrO-STO-113 are shown in Figure 6 (a). Upon the binding, the 4*d* orbital of the interfacial Pd and the 2*p* orbital of O in the first layer of the substrate hybridize; the antibonding Pd $4d_{3z^2-r^2}$ and $4d_{yz}$ orbitals are lifted up to become partially empty; while the Pd $4d_{x^2-y^2}$ orbital is stabilized because of the attractive electrostatic interactions with Sr^{2+} ions of the substrate (Figures 4 (b) and S19 as well as Δq_{L} in Table 2). This intra-unit polarization of Pd atoms makes two contributions to enhance the cluster-substrate binding. The first is to reduce the repulsion originating from the antibonding counterparts of the (Pd 4*d*) - (O 2*p*) hybridized states. The second involves the fact that this polarization generates electrostatic attractions with the substrate Sr cations, which further strengthens the cluster-substrate interactions.

Upon cluster oxidation, Pd_9O_{11} binds to SrO-STO-113 via both Pd - surface O and O -

surface Sr bonds. Both inter-unit CT and intra-unit polarization are significantly enhanced when Pd_9O_{11} is formed. Table 2 shows that increase in population of interfacial Pd $5sp$ orbitals in Pd_9O_{11} is less than that in Pd_9, while O $2p$ orbitals are further populated by bonding with surface Sr. PDOS in Figure 6(b) illustrates that Pd forms strongly hybridized states with surface O, as shown by the large splitting in the PDOS of $4d$ states compared with the PDOS of the metallic cluster. The antibonding Pd $4d_{3z^2-r^2}$ orbital of Pd_9O_{11} is more empty than that of Pd_9 (Table 2), and thus, the Pauli repulsion derived from the those orbitals hybridization is diminished upon cluster oxidation. Moreover, the polarization of interfacial Pd $4d$ electrons in Pd_9O_{11} stabilizes Pd $4d_{xz}$ and $4d_{xy}$ orbitals via electrostatic interactions with surface Sr cations (see the projection of $\Delta\rho$ (5) in Figure 4 (c)). This polarization stabilizes the Pd t_{2g} states of Pd_9O_{11} compared with that of Pd_9. Together with the Pd-O bond, cluster O atoms strongly bind to the surface Sr cations underneath and a considerable electron donation occurs from Sr to O as seen by the downshift of cluster O $2p_z$ below the Fermi level (Figure 6 (b)). Overall, the enhanced Pd-O bonds and newly formed O-Sr bonds explain why MSI increases upon the cluster oxidation on STO supports.

It is important to clarify the difference in the binding strength of Pd_xO_y to γ-Al_2O_3 and STO. We find that the greater CT interaction is the main origin for stronger binding of Pd_xO_y to SrO-STO-113 than that to γ-Al_2O_3. Moreover, the Pd $4d$ polarization, which occurs to a greater extent due to electrostatic attractions with surface Sr cations in Pd_xO_y/SrO-STO-113, also enhances the cluster binding strength. This can be seen clearly in $\Delta\rho$ maps of Pd_9/SrO-STO-113 (Figure 4 (b)) and Pd_9/γ-Al_2O_3(100) (Figure S22), where the charge accumulation in xy plane of Pd atom in Pd_9/γ-Al_2O_3(100) is absent.

Roles of defects and different facets

The current insights into MSI of Pd cluster pertain to the most stable STO-327(001) surface. The surface defects[87] or different surface facet[88,89] may stabilize Pd clusters. We explore the surface defects (V_O, V_{Sr}, and V_{Ti}), the STO-327 facets, and Pd solid solution on the binding

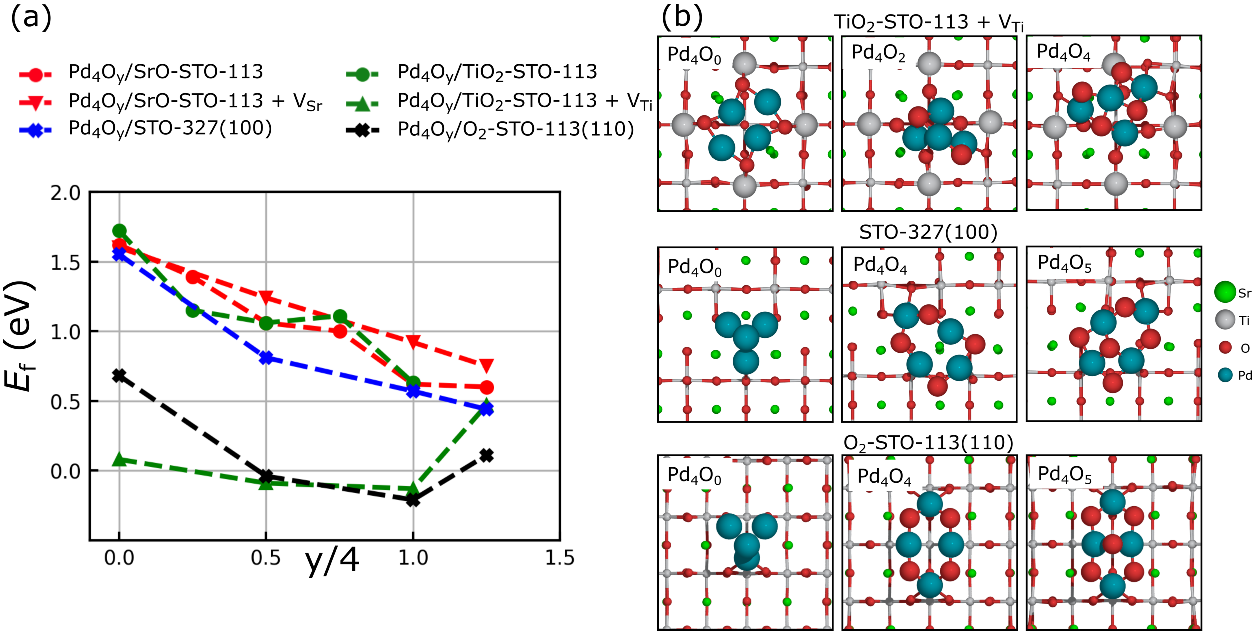

Figure 7: (a) Formation energies (E_f) of $\mathrm{Pd_4O}_y$ on SrO-STO-113 with the surface V_Sr (SrO-STO-113 + V_Sr), $\mathrm{TiO_2}$-STO-113 with the surface V_Ti ($\mathrm{TiO_2}$-STO-113 + V_Ti), STO-327(100), and stoichiometric O-terminated STO-113 (110) [$\mathrm{O_2}$-STO-113(110)]. (b) Atomic geometries of stable $\mathrm{Pd_4O}_y$ supported on $\mathrm{TiO_2}$-STO-113 + V_Ti, STO-327(100), and $\mathrm{O_2}$-STO-113(110).

strengths of the Pd clusters. From Figure 3, E_f's of $\mathrm{Pd_9O}_y$ with $y > 4$ (3) for SrO-STO-113 ($\mathrm{TiO_2}$-STO-113) surpass that of $\mathrm{Pd_9}$ and O-deficient STO-113 surfaces ($\mathrm{Pd_9}$+$\mathrm{V_O}$, star symbols). Therefore, the oxidation of the Pd cluster has a more pronounced role in improving the binding strength of Pd clusters compared with formation of V_O. From Figure 7, E_f's of $\mathrm{Pd_4O}_y$ is slightly increased upon the formation of surface V_Sr for SrO-STO-113 ($\mathrm{Pd_4O}_y$ + $\mathrm{V_{Sr}}$), indicating that formation of $\mathrm{V_{Sr}}$ decreases the binding strengths of the Pd clusters. In contrast, E_f's of $\mathrm{Pd_4O_2}$ and $\mathrm{Pd_4O_4}$ on $\mathrm{TiO_2}$-STO-113 + V_Ti are -0.08 and -0.13 eV, respectively, showing that Pd clusters prefer to bind to Ti vacancy of $\mathrm{TiO_2}$-STO-113. Our results show that Pd clusters might be (partially) embedded in the $\mathrm{TiO_2}$-STO-113 substrate to enhance the sintering resistance.[14]

The binding strengths of $\mathrm{Pd_4O}_y$ to different STO facets, namely STO-327(001) and stoichiometric O-terminated STO-113(110) [$\mathrm{O_2}$-STO-113(110)],[89] are shown in Figure 7. Comparing with the results on SrO- and $\mathrm{TiO_2}$-STO-113, the binding strengths of $\mathrm{Pd_4O}_y$ are slightly increased on STO-327(001), where the $\mathrm{Pd_4O}_y$ clusters prefer to bind to STO-327(001) at the SrO rock salt layer position. On the other hand, Pd_4O_y clusters strongly bind to O_2-STO-113(110), and E_f of Pd_4O_4 is negative. It indicates that the Pd clusters can be trapped effectively on STO-113(110).

We study the stability of oxidized Pd_9O_y ($y = 9, 11$) on the surface of the solid solution (SrO-B-PdO_2), which is realized under oxidative SrO rich conditions. The stability of those oxidized Pd clusters slightly decreases upon Pd solid solution for the TiO_2 subsurface of SrO-STO-113 (See section SVI of SI).

Finally, we note that the effect of migration of the support onto the Pd NPs to form thin overlayers is not considered herein because the metal NP with small size is difficult to be encapsulated by the substrate immigration.[90]

Phase diagram of Pd_9O_y clusters on the STO supports

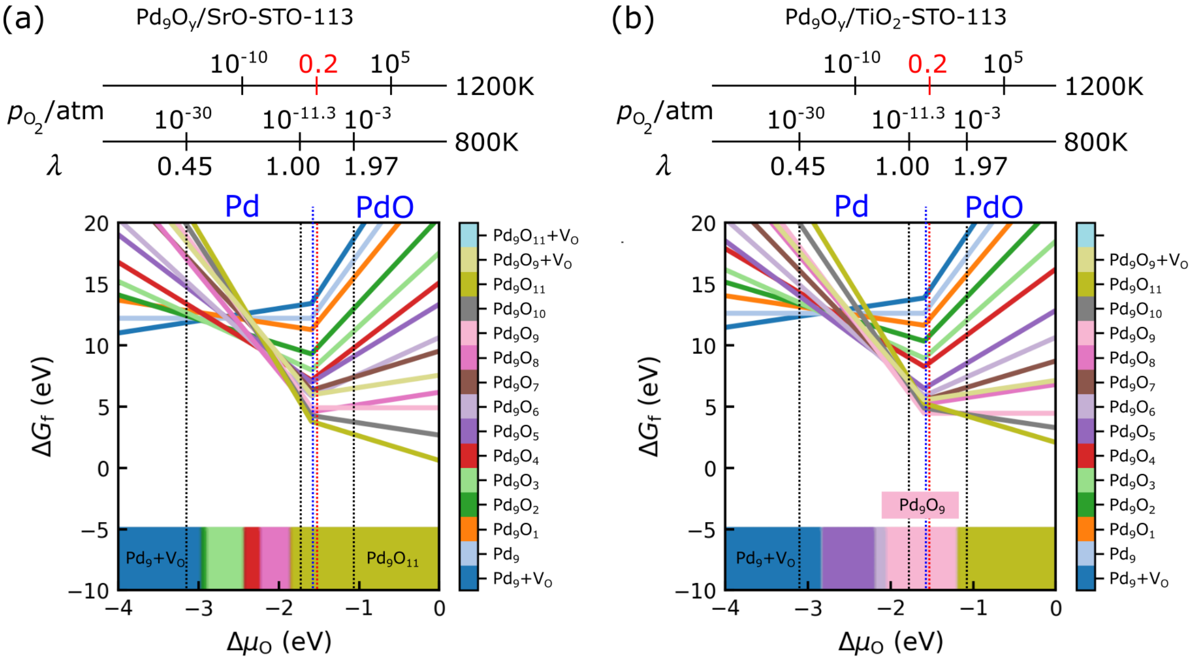

Figure 8: Free energy of formation ΔG_f as a function of relative O chemical potential $\Delta\mu_O$ for Pd_9O_y supported on (a) SrO- and (b) TiO_2-STO-113. The most stable compositions are indicated by the corresponding colors (see the legend) at the bottom of the box. The black, red, and blue vertical lines denote the typical $\Delta\mu_O$ under TWC operating, air-aging, and bulk Pd/PdO phase equilibrium conditions, respectively.

We discuss how TWC operating conditions change the stoichiometry of the Pd_9O_y clusters. We choose Pd_9O_y clusters because they resemble Pd NPs.[68] Stable Pd_9O_y clusters are indicated by phase diagrams in Figures 8 (a) and (b) for Pd_9O_y on SrO- and TiO_2- STO-113, respectively.

In the TWC fuel-rich atmosphere, metallic Pd_9 clusters with V_O formation at the support surfaces (Pd_9+V_O) are stable on both SrO- and TiO_2-STO-113 (Figures 8 (a) and (b)). On clean surfaces, the V_O formation requires an extremely reductive condition ($\Delta\mu_O \leq -4.45[-5.54]$ eV for TiO_2- [SrO-] terminated surfaces). The metallic Pd clusters catalyze the V_O formation at a higher $\Delta\mu_O$ of -3.0 eV for both surfaces, which can occur spontaneously under the TWC reductive condition. Binding strengths (E_f's) of Pd_9's on the O-deficient STO surfaces are enhanced and those clusters are further negatively charged when V_O's are formed (Figure 3). These indicate that the V_O acts like the anchoring site to stabilize the supported Pd NPs in reductive conditions[91] and enhances the CT from the support.[92]

Partially oxidized Pd_9 clusters, where O atoms are adsorbed on them, are stable under rather reductive conditions ($-2.8 < \Delta\mu_O < -2.1$ eV). From Figure 8, Pd_9O_3 and Pd_9O_5 are stable on SrO-STO-113 with $-2.80 < \Delta\mu_O < -2.20$ eV; while Pd_9O_5 and Pd_9O_6 are stable on TiO_2-STO-113 with $-2.84 < \Delta\mu_O < -2.08$ eV.

Under TWC stoichiometric ($\Delta\mu_O = -1.74$ eV), air-aging ($\Delta\mu_O = -1.42$ eV), and fuel-lean ($\Delta\mu_O = -1.08$ eV) conditions, PdO-like clusters are stable, in line with experimental observation.[25] The supported PdO-like clusters are stable when $\Delta\mu_O \geq -2.00$ eV, while the isolated PdO-like Pd_9O_y ($y \geq 9$) clusters and bulk PdO are stable when $\Delta\mu_O \geq -1.30$ eV (Figure S24) and -1.59 eV, respectively. Thus, the STO support stabilizes the high oxidation state of Pd, which arises from the strong interaction between PdO-like clusters and supports.[21,56,78] The stability of PdO-like clusters on the STO support in the fuel-lean and air-aging atmospheres indicates that the sintering resistance is governed by those clusters. Our results highlight the importance of the support materials in regulating the oxidation state of metal catalysts.[21,56,78]

Growth of supported PdO-like clusters

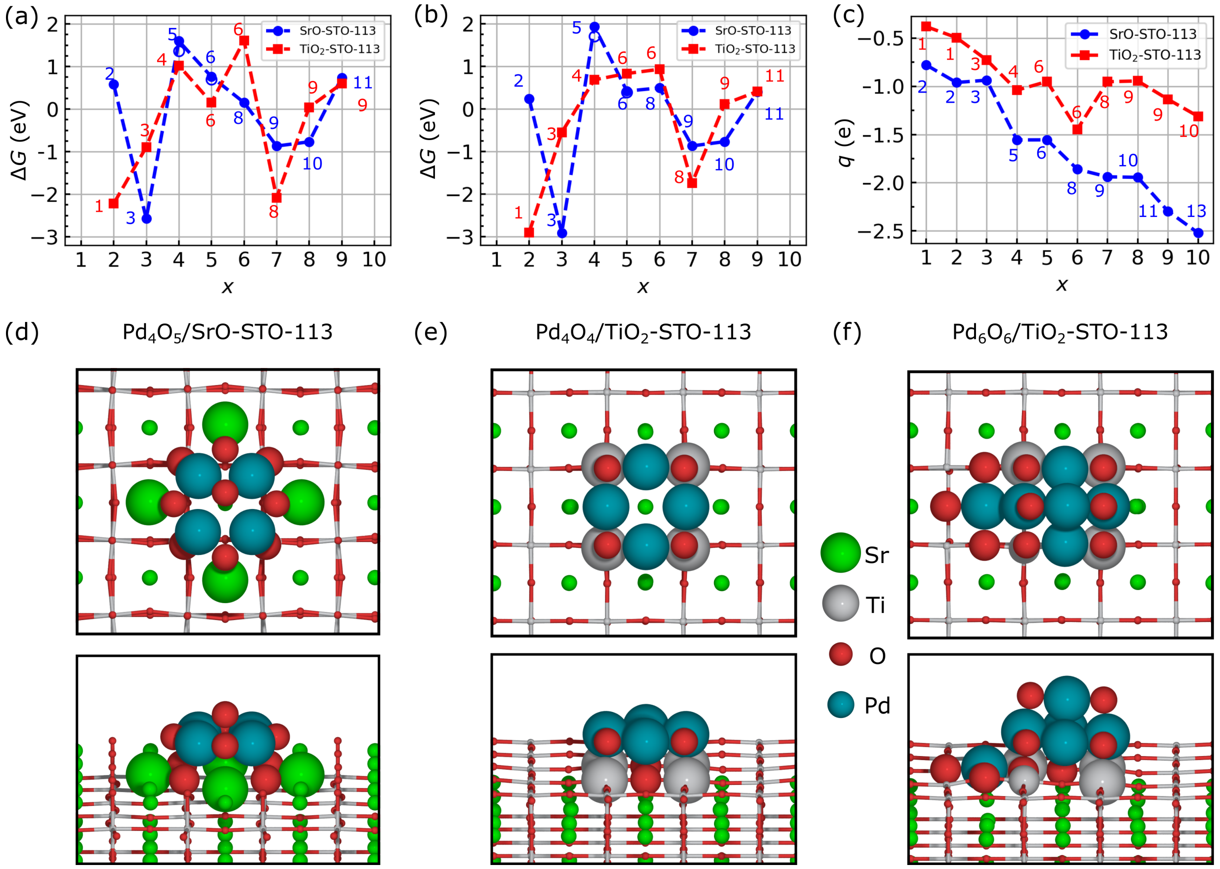

Figure 9: Reaction free energy (ΔG) of the first step of a monodisperse system sintering via the Ostwald ripening of Pd_xO_y as a function of the number of Pd atoms under (a) the air-aging condition ($T = 1200$ K and $p_{O_2} = 0.2$ atm) and (b) the fuel-lean condition ($T = 800$ K and $p_{O_2} = 10^{-3}$ atm). The ΔG with the vibrational contribution of Pd_xO_y clusters (Pd_4O_5 and Pd_5O_6) are shown in the open blue circle. (c) The effective charge (q) of the most stable Pd_xO_y under air-aging condition. The number near each point shows y of the most stable Pd_xO_y. Atomic structures of (d) Pd_4O_5/SrO-STO-113, (e) Pd_4O_4/TiO_2-STO-113, and (f) Pd_6O_6/TiO_2-STO-113, which are stable against the sintering via the Otsward ripening.

Finally, we discuss the growth mechanism of small PdO-like Pd_xO_y clusters supported on STO surfaces in oxidative atmospheres. Small NPs with the size of ≤ 2 nm sinter more easily,[2,93,94] and thus understanding the growth mechanism of NP at the sub-nano regime is beneficial to design an acquisition strategy that prevents the rapid loss of subnanometer NPs. The most stable cluster at each cluster size of the PdO-like clusters is evaluated by comparing ΔG_{f} ($Pd_xO_{x,\,x+1,\,x+2}$). First, we evaluate the detachment free energy (G_{det})

of $\mathrm{Pd}_x\mathrm{O}_y$ in SrO-STO-113 under TWC fuel-lean condition, i.e. the free energy change of the reaction: $\mathrm{Pd}_x\mathrm{O}_y + 1/2(y_1 + 2 - y)\ \mathrm{O}_2 \rightarrow \mathrm{Pd}_{x-1}\mathrm{O}_{y1} + \mathrm{PdO}_2$. Moreover, we investigate activation energies for diffusion of PdO_2, $\mathrm{Pd}_2\mathrm{O}_2$, $\mathrm{Pd}_3\mathrm{O}_3$, and $\mathrm{Pd}_4\mathrm{O}_5$ on SrO-STO-113. Those results are shown in Figure S33. We find that the detachment of PdO_2 from $\mathrm{Pd}_x\mathrm{O}_y$, which is relevant to the Ostward ripening, is more preferable than the particle diffusion, which is relevant to coalescence.[87] An analogous observation is made for TiO_2-STO-113. The growth of PdO-like clusters thus may follow the Ostward ripening, i.e., the migration of atomic species from smaller to larger NPs at the sub-nano regime.[87] The activation energies for diffusion of the small clusters ($x < 4$) are less than 2 eV (Figure S33). Using a lattice-hop model,[95] the diffusion of a particle with an activation energy of 2.0 eV occurs at $T > 700$K. Thus, the coalescence mechanism is still possible for those small $\mathrm{Pd}_x\mathrm{O}_y$ clusters ($x < 4$).

At a fixed chemical potential, the stability of $\mathrm{Pd}_x\mathrm{O}_y$ can be estimated by considering the first step of a monodisperse system sintering via Ostward ripening[96,97] as

$$2\mathrm{Pd}_x\mathrm{O}_y + \frac{1}{2}(y_1 + y_2 - y)\mathrm{O}_2 \rightarrow \mathrm{Pd}_{x-1}\mathrm{O}_{y_1} + \mathrm{Pd}_{x+1}\mathrm{O}_{y_2}, \tag{6}$$

and the reaction free energy is calculated by

$$\Delta G(x) = E(\mathrm{Pd}_{x-1}\mathrm{O}_{y_1}/S) + E(\mathrm{Pd}_{x+1}\mathrm{O}_{y_2}/S) - 2E(\mathrm{Pd}_x\mathrm{O}_y/S) - (y_1 + y_2 - y)\mu_\mathrm{O}, \tag{7}$$

where $E(\mathrm{Pd}_{x-1}\mathrm{O}_{y_1}/S)$, $E(\mathrm{Pd}_{x+1}\mathrm{O}_{y_2}/S)$, and $E(\mathrm{Pd}_x\mathrm{O}_y/S)$ are the total energies of the supported $\mathrm{Pd}_{x-1}\mathrm{O}_{y_1}$, $\mathrm{Pd}_{x+1}\mathrm{O}_{y_2}$, and $\mathrm{Pd}_x\mathrm{O}_y$, respectively. $\Delta G(x)$ is estimated using only the global minimum for each $\mathrm{Pd}_x\mathrm{O}_y$ cluster, which provides a reasonable explanation for size dependence.[96] A positive $\Delta G(x)$ indicates that $\mathrm{Pd}_x\mathrm{O}_y$ is stable and its growth is less preferable. The contribution of cluster vibrational entropy in $\Delta G(x)$ is negligible because it plays a minor role (Figure 9 (a) and (b)).

Figures 9 (a) and (b) shows the calculated ΔG's for air-aging and fuel-lean conditions at $\Delta\mu_\mathrm{O} = -1.42$ and -1.08 eV, respectively, as a function of the number of Pd atoms in the cluster. The effective charges (q's) of the most stable Pd_xO_y's under the air-aging condition are shown in Figure 9 (c). The corresponding atomic structures for SrO- and TiO_2-STO-113 are shown in Figures S35 and S36, respectively. The ΔG's for certain cluster sizes are positive, which indicate that they are stable against Ostwald ripening and the cluster growth may be diminished.[96,97] The largest ΔG's are found for Pd_4O_5 on SrO-STO-113, and Pd_4O_4 and Pd_6O_6 on TiO_2-STO-113 under the air-aging condition. Similarly, the largest ΔG's are found for Pd_4O_5 on SrO-STO-113 and Pd_6O_6 on TiO_2-STO-113 under the oxidative condition. Thus, Pd_4O_5 on SrO-STO-113, and Pd_4O_4 and Pd_6O_6 on TiO_2-STO-113 are called magic number clusters.[96,97]

The stability of the magic number clusters can be understood from their geometries (Figures S35 and S36). The Pd_4O_5 (Pd_4O_4) cluster on SrO-STO-113 (TiO_2-STO-113) has a monolayer geometry with all Pd atoms bonding to the substrate O atoms, as shown in Figure 9 (d) (Figure 9 (e)). The growth of Pd_4O_5 (Pd_4O_4) may be realized by adding PdO (PdO_2) to form Pd_5O_6 in a bilayer geometry with the same number of the interfacial Pd-O bonds. The charge transfer to the additional PdO (PdO_2) is negligibly small and does not contribute to the stabilization of the larger Pd_5O_6 (Figure 9 (c)). In the case of Pd_6O_6 on TiO_2-STO-113, the cluster can be considered as Pd_5O_6 plus a Pd atom residing next to the cluster. The additional Pd atom creates an additional interfacial Pd-O bond, which results in a significant CT (Figure 9 (c)) and stabilizes the cluster.

Overall, our results indicate that oxidation of the Pd clusters strengthens the interfacial bonds of the Pd_xO_y cluster. This lowers the mobility of Pd_xO_y by increasing the activation energy for diffusion and triggers the Ostward ripening by lowering the free energy of detachment. The activation energies for diffusion of Pd_4O_5 and PdO_2 on SrO-STO-113 are 3.13 and 0.82 eV, respectively, which are higher than that of Pd_4 and a Pd adatom (1.52 and 0.50 eV, respectively). On the other hand, free energies of detachment of PdO-like clusters are slightly lower than that of metallic Pd_x (Figure S33). Our finding is consistent with the Sabatier principle proposed by Li et al.[83] where a stronger MSI lowers the mobility and stimulates the Ostward ripening.

Chemical potentials of the PdO-like NPs in the hemispherical shape supported on SrO-STO-113 and γ-Al_2O_3(100) are elucidated based on Campbell-Mao equation[98] to highlight the role of MSI in the NP size. We find that the growth of the PdO-like NP is almost diminished on SrO-STO-113 with the size of 4 nm, while the sintering trend on γ-Al_2O_3(100) is still rapid with the size of 4 nm (See section SXII of SI).

Conclusion

In summary, we demonstrated that supported oxidized Pd_xO_y particles on STO-327 fulfill the conditions for the self-regenerative catalyst by elucidating their MSI under the TWC operating conditions by using DFT calculations combined with GOFEE and thermodynamics. First, the Pd solid solution is found to be preferable in the oxidative atmosphere. But the rock-salt SrO layer was predicted to have ability to mitigate the penetration of Pd from STO-327(001) to bulk region, leading to SSR suppression. Second, we showed that PdO-like clusters strongly bind to support surfaces, which implies that the cluster oxidation can improve the thermal stability against sintering. The effects of the oxide support and cluster size on cluster stability were revealed where the CT interactions play an important role. Our findings provide unique insights into the role of the metal oxidation state and support interactions in the stability of supported metal clusters, which may be useful for the development of sintering resistant TWC's.

Supporting Information Available

Preliminaries and calculation details; Crystal structures of Pd@STO-327 and and phonon analysis; Surface stability of STO-327 (001) at SrO and TiO_2 precipitation lines; Atomic geometries of supported Pd_xO_y; Slab thickness dependence on the formation energy of the supported Pd_9O_y; Role of solid solution of Pd in stabilization of small Pd clusters; Bonding nature of Pd clusters with SrO-STO-113 surface; Stability of gas-phased Pd_9O_y; Diffusion and detachment of supported oxidized clusters; Atomic structures of the most stable Pd_xO_y under the air-aging conditions; Size dependence of PdO-like nanoparticle

Acknowledgement

We thank Professors Saburo Hosokawa and Tsunehiro Tanaka for providing their experimental results prior to publication, and for their discussions. We are also indebted to Professors Shigeyoshi Sakaki and Masahiro Ehara for their valuable discussions; and to Dr. Malthe K. Bisbo and Professor Bjørk Hammer for their introduction to the GOFEE method. This work was supported by Grants-in-Aid for Transformative Research Areas (A) "Hyper-Ordered Structure Science" (Grant No. JP20H05883), for Scientific Research (B) (Grant No. JP20H02569), for Scientific Research (C) (Grant No. JP21K03419), and for JSPS Fellows (21J10648) from the Japan Society for the Promotion of Science (JSPS), and by Elements Strategy Initiative for Catalysts and Batteries (ESICB) (Grant No. JPMXP0112101003) from the Ministry of Education, Culture, Sports, Science, and Technology, Japan (MEXT). T.N.P. gratefully acknowledges financial supports from MEXT and Professional Development Consortium for Computational Materials Scientists - Innovative Professional Development Program (PCoMS-IPD). The computations were performed using computer resources at the Research Center for Computational Science, Okazaki; the Cyberscience Center, Tohoku University; the Center for Computational Materials Science, Institute for Materials Research; Tohoku University; the Institute for Solid State Physics, University of Tokyo.

References

(1) Dai, Y.; Lu, P.; Cao, Z.; Campbell, C. T.; Xia, Y. The physical chemistry and materials science behind sinter-resistant catalysts. *Chem. Soc. Rev* **2018**, *47*, 4314–4331.

(2) Goodman, E. D.; Schwalbe, J. A.; Cargnello, M. Mechanistic understanding and the rational design of sinter-resistant heterogeneous catalysts. *ACS Catal.* **2017**, *7*, 7156–7173.

(3) Ahmadi, M.; Mistry, H.; Roldan Cuenya, B. Tailoring the catalytic properties of metal nanoparticles via support interactions. *J. Phys. Chem. Lett.* **2016**, *7*, 3519–3533.

(4) van Deelen, T. W.; Hernández Mejía, C.; de Jong, K. P. Control of metal-support interactions in heterogeneous catalysts to enhance activity and selectivity. *Nat. Catal.* **2019**, *2*, 955–970.

(5) Taylor, K. C. Nitric oxide catalysis in automotive exhaust systems. *Catal. Rev.: Sci. Eng.* **1993**, *35*, 457–481.

(6) Shelef, M.; Graham, G. Why rhodium in automotive three-way catalysts? *Catal. Rev.: Sci. Eng.* **1994**, *36*, 433–457.

(7) Asakura, H.; Hosokawa, S.; Ina, T.; Kato, K.; Nitta, K.; Uera, K.; Uruga, T.; Miura, H.; Shishido, T.; Ohyama, J.; others Dynamic behavior of Rh species in Rh/Al_2O_3 model catalyst during three-way catalytic reaction: An operando X-ray absorption spectroscopy study. *J. Am. Chem. Soc.* **2018**, *140*, 176–184.

(8) Asakura, H.; Hosokawa, S.; Beppu, K.; Tamai, K.; Ohyama, J.; Shishido, T.; Kato, K.; Teramura, K.; Tanaka, T. Real-time observation of the effect of oxygen storage materials on Pd-based three-way catalysts under ideal automobile exhaust conditions: An operando study. *Catal. Sci. Technol.* **2021**, *11*, 6182–6190.

(9) Ding, C.; Gu, Q.; Yu, L.-J.; Zhang, S.; Zhang, Y.; Ma, Z.; Meng, Y.; Zhang, H.; Wang, T.; Wang, J.; others Reversible transformation and distribution determination of diverse Pt single-atom species. *J. Am. Chem. Soc.* **2023**, *145*, 2523–2531.

(10) Nishihata, Y.; Mizuki, J.; Akao, T.; Tanaka, H.; Uenishi, M.; Kimura, M.; Okamoto, T.; Hamada, N. Self-regeneration of a Pd-perovskite catalyst for automotive emissions control. *Nature* **2002**, *418*, 164–167.

(11) Tang, K.; Ren, Y.; Liu, W.; Wei, J.; Guo, J.; Wang, S.; Yang, Y. Insight investigation of active palladium surface sites in palladium-ceria Catalysts for NO+ CO reaction. *ACS Appl. Mater. Interfaces* **2018**, *10*, 13614–13624.

(12) Machida, M.; Uchida, Y.; Ishikawa, Y.; Hinokuma, S.; Yoshida, H.; Ohyama, J.; Nagao, Y.; Endo, Y.; Iwashina, K.; Nakahara, Y. Thermostable Rh metal nanoparticles formed on Al_2O_3 by high-temperature H_2 reduction and its impact on three-way catalysis. *J. Phys. Chem. C* **2019**, *123*, 24584–24591.

(13) Machida, M.; Uchida, Y.; Iwashita, S.; Yoshida, H.; Tsushida, M.; Ohyama, J.; Nagao, Y.; Endo, Y.; Wakabayashi, T. Catalyst deactivation via rhodium–support interactions under high-temperature oxidizing conditions: a comparative study on hexaaluminates versus Al_2O_3. *ACS Catal.* **2021**, *11*, 9462–9470.

(14) Kothari, M.; Jeon, Y.; Miller, D. N.; Pascui, A. E.; Kilmartin, J.; Wails, D.; Ramos, S.; Chadwick, A.; Irvine, J. T. Platinum incorporation into titanate perovskites to deliver emergent active and stable platinum nanoparticles. *Nat. Chem.* **2021**, *13*, 677–682.

(15) Machida, M.; Iwashita, S.; Sato, T.; Yoshida, H.; Ohyama, J.; Yoshioka, M.; Miwa, S.; Hashishin, T. Anisotropic Rh^{3+} Diffusion in Layered Hexaaluminate Mitigates Thermal Deactivation of Supported Rhodium Catalysts. *J. Phys. Chem C* **2022**, *126*, 17608–17617.

(16) Neagu, D.; Tsekouras, G.; Miller, D. N.; Ménard, H.; Irvine, J. T. In situ growth of nanoparticles through control of non-stoichiometry. *Nat. Chem.* **2013**, *5*, 916–923.

(17) Neagu, D.; Papaioannou, E. I.; Ramli, W. K.; Miller, D. N.; Murdoch, B. J.; Ménard, H.; Umar, A.; Barlow, A. J.; Cumpson, P. J.; Irvine, J. T.; others Demonstration of chem-

istry at a point through restructuring and catalytic activation at anchored nanoparticles. *Nat. Commun* **2017**, *8*, 1–8.

(18) Machida, M.; Eidome, T.; Minami, S.; Buwono, H. P.; Hinokuma, S.; Nagao, Y.; Nakahara, Y. Tuning the electron density of Rh supported on metal phosphates for three-way catalysis. *J. Phys. Chem. C* **2015**, *119*, 11653–11661.

(19) Lai, K.-Y.; Manthiram, A. Evolution of exsolved nanoparticles on a perovskite oxide surface during a redox process. *Chem. Mater.* **2018**, *30*, 2838–2847.

(20) Machida, M. Heat-and corrosion-resistant catalytic materials for environmental and energy applications. *J. Ceram. Soc. Japan* **2021**, *129*, 234–240.

(21) Nagai, Y.; Hirabayashi, T.; Dohmae, K.; Takagi, N.; Minami, T.; Shinjoh, H.; Matsumoto, S. Sintering inhibition mechanism of platinum supported on ceria-based oxide and Pt-oxide–support interaction. *J. Catal.* **2006**, *242*, 103–109.

(22) Nagai, Y.; Dohmae, K.; Ikeda, Y.; Takagi, N.; Tanabe, T.; Hara, N.; Guilera, G.; Pascarelli, S.; Newton, M. A.; Kuno, O.; others In situ redispersion of platinum autoexhaust catalysts: an on-line approach to increasing catalyst lifetimes? *Angew. Chem. Int. Ed.* **2008**, *47*, 9303–9306.

(23) Shinjoh, H.; Hatanaka, M.; Nagai, Y.; Tanabe, T.; Takahashi, N.; Yoshida, T.; Miyake, Y. Suppression of noble metal sintering based on the support anchoring effect and its application in automotive three-way catalysis. *Top Catal.* **2009**, *52*, 1967–1971.

(24) Nur, A. S.; Funada, E.; Kiritoshi, S.; Matsumoto, A.; Kakei, R.; Hinokuma, S.; Yoshida, H.; Machida, M. Phase-dependent formation of coherent interface structure between PtO_2 and TiO_2 and its impact on thermal decomposition behavior. *J. Phys. Chem. C* **2018**, *122*, 662–669.

(25) Beppu, K.; Demizu, A.; Hosokawa, S.; Asakura, H.; Teramura, K.; Tanaka, T. Pd/$SrFe_{1-x}Ti_xO_{3-\delta}$ as environmental catalyst: Purification of automotive exhaust gases. *ACS Appl. Mater. Interfaces* **2018**, *10*, 22182–22189.

(26) Machida, M.; Fujiwara, A.; Yoshida, H.; Ohyama, J.; Asakura, H.; Hosokawa, S.; Tanaka, T.; Haneda, M.; Tomita, A.; Miki, T.; others Deactivation mechanism of Pd/CeO_2–ZrO_2 three-way catalysts analyzed by chassis-dynamometer tests and in situ diffuse reflectance spectroscopy. *ACS Catal.* **2019**, *9*, 6415–6424.

(27) Bruix, A.; Lykhach, Y.; Matolínová, I.; Neitzel, A.; Skála, T.; Tsud, N.; Vorokhta, M.; Stetsovych, V.; Ševčíková, K.; Mysliveček, J.; others Maximum noble-metal efficiency in catalytic materials: atomically dispersed surface platinum. *Angew. Chem., Int. Ed.* **2014**, *53*, 10525–10530.

(28) Gatla, S.; Aubert, D.; Agostini, G.; Mathon, O.; Pascarelli, S.; Lunkenbein, T.; Willinger, M. G.; Kaper, H. Room-temperature CO oxidation catalyst: low-temperature metal–support interaction between platinum nanoparticles and nanosized ceria. *ACS Catal.* **2016**, *6*, 6151–6155.

(29) Lee, J.; Ryou, Y.; Chan, X.; Kim, T. J.; Kim, D. H. How Pt interacts with CeO_2 under the reducing and oxidizing environments at elevated temperature: the origin of improved thermal stability of Pt/CeO_2 compared to CeO_2. *J. Phys. Chem. C* **2016**, *120*, 25870–25879.

(30) Shingai, K.; Tanabe, T.; Hosokawa, S.; Asakura, H.; Naniwa, S.; Iguchi, S.; Teramura, K.; Tanaka, T. Catalytic activity of Pd catalyst supported on $Sr_3Ti_2O_7$ for purifying automotive exhaust gases In *Book of Abstracts, 2022 Osaka-Kansai International Symposium on Catalysis (OKCAT2022)*,Osaka, Japan;

(31) Giannozzi, P.; Baroni, S.; Bonini, N.; Calandra, M.; Car, R.; Cavazzoni, C.; Ceresoli, D.; Chiarotti, G. L.; Cococcioni, M.; Dabo, I.; others QUANTUM ESPRESSO: A modular

and open-source software project for quantum simulations of materials. *J. Condens. Matter Phys* **2009**, *21*, 395502.

(32) Perdew, J. P.; Ruzsinszky, A.; Csonka, G. I.; Vydrov, O. A.; Scuseria, G. E.; Constantin, L. A.; Zhou, X.; Burke, K. Restoring the density-gradient expansion for exchange in solids and surfaces. *Phys. Rev. Lett.* **2008**, *100*, 136406.

(33) Vanderbilt, D. Soft self-consistent pseudopotentials in a generalized eigenvalue formalism. *Phys. Rev. B* **1990**, *41*, 7892.

(34) Dal Corso, A. Pseudopotentials periodic table: From H to Pu. *Comput. Mater. Sci.* **2014**, *95*, 337–350.

(35) Cococcioni, M.; De Gironcoli, S. Linear response approach to the calculation of the effective interaction parameters in the LDA+ U method. *Phys. Rev. B* **2005**, *71*, 035105.

(36) Ricca, C.; Timrov, I.; Cococcioni, M.; Marzari, N.; Aschauer, U. Self-consistent DFT+$U + V$ study of oxygen vacancies in $SrTiO_3$. *Phys. Rev. Res.* **2020**, *2*, 023313.

(37) Wang, L.; Maxisch, T.; Ceder, G. Oxidation energies of transition metal oxides within the GGA+U framework. *Phys. Rev. B* **2006**, *73*, 195107.

(38) Grimme, S.; Antony, J.; Ehrlich, S.; Krieg, H. A consistent and accurate ab initio parametrization of density functional dispersion correction (DFT-D) for the 94 elements H-Pu. *J. Chem. Phys.* **2010**, *132*, 154104.

(39) Grimme, S.; Ehrlich, S.; Goerigk, L. Effect of the damping function in dispersion corrected density functional theory. *J. Comput. Chem.* **2011**, *32*, 1456–1465.

(40) Monkhorst, H. J.; Pack, J. D. Special points for Brillouin-zone integrations. *Phys. Rev. B* **1976**, *13*, 5188.

(41) Jónsson, H.; Mills, G.; Jacobsen, K. W. *Classical and quantum dynamics in condensed phase simulations*; World Sci., 1998; pp 385–404.

(42) Henkelman, G.; Uberuaga, B. P.; Jónsson, H. A climbing image nudged elastic band method for finding saddle points and minimum energy paths. *J. Chem. Phys* **2000**, *113*, 9901–9904.

(43) Löwdin, P.-O. On the non-orthogonality problem connected with the use of atomic wave functions in the theory of molecules and crystals. *J. Chem. Phys* **1950**, *18*, 365–375.

(44) Digne, M.; Sautet, P.; Raybaud, P.; Euzen, P.; Toulhoat, H. Use of DFT to achieve a rational understanding of acid–basic properties of γ-alumina surfaces. *J. Catal.* **2004**, *226*, 54–68.

(45) Togo, A.; Oba, F.; Tanaka, I. First-principles calculations of the ferroelastic transition between rutile-type and $CaCl_2$-type SiO_2 at high pressures. *Phys. Rev. B* **2008**, *78*, 134106.

(46) Reuter, K.; Scheffler, M. Composition, structure, and stability of RuO_2 (110) as a function of oxygen pressure. *Phys. Rev. B* **2001**, *65*, 035406.

(47) Bjørheim, T. S.; Arrigoni, M.; Gryaznov, D.; Kotomin, E.; Maier, J. Thermodynamic properties of neutral and charged oxygen vacancies in $BaZrO_3$ based on first principles phonon calculations. *Phys. Chem. Chem. Phys.* **2015**, *17*, 20765–20774.

(48) Heifets, E.; Piskunov, S.; Kotomin, E. A.; Zhukovskii, Y. F.; Ellis, D. E. Electronic structure and thermodynamic stability of double-layered $SrTiO_3$ (001) surfaces: Ab initio simulations. *Phys. Rev. B* **2007**, *75*, 115417.

(49) Yanagisawa, S.; Uozumi, A.; Hamada, I.; Morikawa, Y. Search for a self-regenerating perovskite catalyst using ab initio thermodynamics calculations. *J. Phys. Chem. C* **2013**, *117*, 1278–1286.

(50) Chase, M. W.; (US), N. I. S. O. *NIST-JANAF thermochemical tables*; American Chemical Society Washington, DC, 1998; Vol. 9.

(51) Machida, M.; Kawada, T.; Fujii, H.; Hinokuma, S. The role of CeO_2 as a gateway for oxygen storage over CeO_2-grafted Fe_2O_3 composite materials. *J. Phys. Chem. C* **2015**, *119*, 24932–24941.

(52) Hirakawa, T.; Shimokawa, Y.; Tokuzumi, W.; Sato, T.; Tsushida, M.; Yoshida, H.; Ohyama, J.; Machida, M. Multicomponent 3d transition-metal nanoparticles as catalysts free of Pd, Pt, or Rh for automotive three-way catalytic converters. *ACS Appl. Nano Mater.* **2020**, *3*, 9097–9107.

(53) Bisbo, M. K.; Hammer, B. Efficient global structure optimization with a machine-learned surrogate model. *Phys. Rev. Lett.* **2020**, *124*, 086102.

(54) Bisbo, M. K.; Hammer, B. Global optimization of atomic structure enhanced by machine learning. *Phys. Rev. B* **2022**, *105*, 245404.

(55) Merte, L. R.; Bisbo, M. K.; Sokolović, I.; Setvín, M.; Hagman, B.; Shipilin, M.; Schmid, M.; Diebold, U.; Lundgren, E.; Hammer, B. Structure of an ultrathin oxide on Pt_3Sn (111) solved by machine learning enhanced global optimization. *Angew. Chem., Int. Ed.* **2022**, e202204244.

(56) Quinlivan Domínguez, J. E.; Neyman, K. M.; Bruix, A. Stability of oxidized states of free-standing and ceria-supported PtO_x particles. *J. Chem. Phys.* **2022**, *157*, 094709.

(57) Christiansen, M.-P. V.; Rønne, N.; Hammer, B. Atomistic global optimization X: A Python package for optimization of atomistic structures. *J. Chem. Phys.* **2022**, *157*, 054701.

(58) Tang, Z.; Hammer, B. Dimerization of dehydrogenated polycyclic aromatic hydrocarbons on graphene. *J. Chem. Phys.* **2022**, *156*, 134703.

(59) Enkovaara, J.; Rostgaard, C.; Mortensen, J. J.; Chen, J.; Dułak, M.; Ferrighi, L.; Gavnholt, J.; Glinsvad, C.; Haikola, V.; Hansen, H.; others Electronic structure calculations

with GPAW: a real-space implementation of the projector augmented-wave method. *J. Phys. Condens. Matter* **2010**, *22*, 253202.

(60) Perdew, J. P.; Burke, K.; Ernzerhof, M. Generalized gradient approximation made simple. *Phys. Rev. Lett.* **1996**, *77*, 3865.

(61) Reichenbach, T.; Walter, M.; Moseler, M.; Hammer, B.; Bruix, A. Effects of Gas-Phase Conditions and Particle Size on the Properties of Cu (111)-Supported Zn_yO_x Particles Revealed by Global Optimization and Ab Initio Thermodynamics. *J. Phys. Chem. C* **2019**, *123*, 30903–30916.

(62) Raman, A. S.; Vojvodic, A. Modeling exsolution of Pt from $ATiO_3$ perovskites (A= Ca/Sr/Ba) using first-principles methods. *Chem. Mater.* **2020**, *32*, 9642–9649.

(63) Ota, T.; Kizaki, H.; Morikawa, Y. Mechanistic Analysis of Oxygen Vacancy Formation and Ionic Transport in $Sr_3Fe_2O_{7-\delta}$. *J. Phys. Chem. C* **2018**, *122*, 4172–4181.

(64) Zschornak, M.; Gemming, S.; Gutmann, E.; Weißbach, T.; Stöcker, H.; Leisegang, T.; Riedl, T.; Tränkner, M.; Gemming, T.; Meyer, D. Surface modeling and chemical solution deposition of $SrO(SrTiO_3)_n$ Ruddlesden–Popper phases. *Acta Mater.* **2010**, *58*, 4650–4659.

(65) Neitzel, A.; Figueroba, A.; Lykhach, Y.; Skala, T.; Vorokhta, M.; Tsud, N.; Mehl, S.; Sevcikova, K.; Prince, K. C.; Neyman, K. M.; others Atomically dispersed Pd, Ni, and Pt species in ceria-based catalysts: Principal differences in stability and reactivity. *J. Phys. Chem. C* **2016**, *120*, 9852–9862.

(66) Colussi, S.; Gayen, A.; Farnesi Camellone, M.; Boaro, M.; Llorca, J.; Fabris, S.; Trovarelli, A. Nanofaceted Pd-O sites in Pd-Ce surface superstructures: Enhanced activity in catalytic combustion of methane. *Angew. Chem., Int. Ed.* **2009**, *48*, 8481–8484.

(67) Machida, M. Rh nanoparticle anchoring on metal phosphates: Fundamental aspects and practical impacts on catalysis. *Chem. Rec.* **2016**, *16*, 2219–2231.

(68) Liu, J.-X.; Su, Y.; Filot, I. A.; Hensen, E. J. A linear scaling relation for CO oxidation on CeO_2-supported Pd. *J. Am. Chem. Soc.* **2018**, *140*, 4580–4587.

(69) Machida, M.; Minami, S.; Ikeue, K.; Hinokuma, S.; Nagao, Y.; Sato, T.; Nakahara, Y. Rhodium nanoparticle anchoring on $AlPO_4$ for efficient catalyst sintering suppression. *Chem. Mater.* **2014**, *26*, 5799–5805.

(70) Sanchez, S. I.; Menard, L. D.; Bram, A.; Kang, J. H.; Small, M. W.; Nuzzo, R. G.; Frenkel, A. I. The emergence of nonbulk properties in supported metal clusters: negative thermal expansion and atomic disorder in Pt nanoclusters supported on γ-Al_2O_3. *J. Am. Chem. Soc.* **2009**, *131*, 7040–7054.

(71) Tang, H.; Su, Y.; Guo, Y.; Zhang, L.; Li, T.; Zang, K.; Liu, F.; Li, L.; Luo, J.; Qiao, B.; others Oxidative strong metal–support interactions (OMSI) of supported platinum-group metal catalysts. *Chem. Sci.* **2018**, *9*, 6679–6684.

(72) Matos, J.; Ono, L.; Behafarid, F.; Croy, J.; Mostafa, S.; DeLaRiva, A.; Datye, A.; Frenkel, A.; Cuenya, B. R. In situ coarsening study of inverse micelle-prepared Pt nanoparticles supported on γ-Al_2O_3: Pretreatment and environmental effects. *Phys. Chem. Chem. Phys.* **2012**, *14*, 11457–11467.

(73) Behafarid, F.; Pandey, S.; Diaz, R. E.; Stach, E. A.; Cuenya, B. R. An in situ transmission electron microscopy study of sintering and redispersion phenomena over size-selected metal nanoparticles: Environmental effects. *Phys. Chem. Chem. Phys.* **2014**, *16*, 18176–18184.

(74) Matthey, D.; Wang, J.; Wendt, S.; Matthiesen, J.; Schaub, R.; Laegsgaard, E.; Hammer, B.; Besenbacher, F. Enhanced bonding of gold nanoparticles on oxidized TiO_2 (110). *Science* **2007**, *315*, 1692–1696.

(75) Farnesi Camellone, M.; Dvořák, F.; Vorokhta, M.; Tovt, A.; Khalakhan, I.; Johánek, V.; Skála, T.; Matolínová, I.; Fabris, S.; Mysliveček, J. Adatom and nanoparticle dynamics on single-atom catalyst substrates. *ACS Catal.* **2022**, *12*, 4859–4871.

(76) Sangnier, A.; Matrat, M.; Nicolle, A.; Dujardin, C.; Chizallet, C. Multiscale approach to the dissociative adsorption of oxygen on a highly dispersed platinum supported on γ-Al_2O_3. *J. Phys. Chem. C* **2018**, *122*, 26974–26986.

(77) Pan, C.-J.; Tsai, M.-C.; Su, W.-N.; Rick, J.; Akalework, N. G.; Agegnehu, A. K.; Cheng, S.-Y.; Hwang, B.-J. Tuning/exploiting strong metal-support interaction (SMSI) in heterogeneous catalysis. *J. Taiwan Inst. Chem. Eng.* **2017**, *74*, 154–186.

(78) Mammen, N.; Spanu, L.; Tyo, E. C.; Yang, B.; Halder, A.; Seifert, S.; Pellin, M. J.; Vajda, S.; Narasimhan, S. Reversing size-dependent trends in the oxidation of copper clusters through support effects. *Eur. J. Inorg. Chem.* **2018**, *2018*, 16–22.

(79) Kacprzak, K. A.; Czekaj, I.; Mantzaras, J. DFT studies of oxidation routes for Pd_9 clusters supported on γ-alumina. *Phys. Chem. Chem. Phys.* **2012**, *14*, 10243–10247.

(80) Matsui, M.; Machida, M.; Sakaki, S. Characterization of $AlPO_4$ (110) Surface in adsorption of Rh dimer and Its comparison with γ-Al_2O_3 (100) Surface: A theoretical study. *J. Phys. Chem. C* **2015**, *119*, 19752–19762.

(81) Bruix, A.; Rodriguez, J. A.; Ramírez, P. J.; Senanayake, S. D.; Evans, J.; Park, J. B.; Stacchiola, D.; Liu, P.; Hrbek, J.; Illas, F. A new type of strong metal–support interaction and the production of H_2 through the transformation of water on Pt/CeO_2 (111) and $Pt/CeO_x/TiO_2$ (110) catalysts. *J. Am. Chem. Soc.* **2012**, *134*, 8968–8974.

(82) Liu, J.-C.; Luo, L.; Xiao, H.; Zhu, J.; He, Y.; Li, J. Metal affinity of support dictates sintering of gold catalysts. *J. Am. Chem. Soc.* **2022**, *144*, 20601–20609.

(83) Hu, S.; Li, W.-X. Sabatier principle of metal-support interaction for design of ultrastable metal nanocatalysts. *Science* **2021**, *374*, 1360–1365.

(84) Qureshi, M.; Garcia-Esparza, A. T.; Jeantelot, G.; Ould-Chikh, S.; Aguilar-Tapia, A.; Hazemann, J.-L.; Basset, J.-M.; Loffreda, D.; Le Bahers, T.; Takanabe, K. Catalytic consequences of ultrafine Pt clusters supported on $SrTiO_3$ for photocatalytic overall water splitting. *J. Catal.* **2019**, *376*, 180–190.

(85) Zachman, M. J.; Fung, V.; Polo-Garzon, F.; Cao, S.; Moon, J.; Huang, Z.; Jiang, D.-e.; Wu, Z.; Chi, M. Measuring and directing charge transfer in heterogenous catalysts. *Nat. Commun.* **2022**, *13*, 3253.

(86) Bagus, P. S.; Staemmler, V.; Wöll, C. Exchangelike effects for closed-shell adsorbates: Interface dipole and work function. *Phys. Rev. Lett.* **2002**, *89*, 096104.

(87) Su, Y.-Q.; Liu, J.-X.; Filot, I. A.; Hensen, E. J. Theoretical study of ripening mechanisms of Pd clusters on ceria. *Chem. Mater.* **2017**, *29*, 9456–9462.

(88) Yuan, W.; Zhang, D.; Ou, Y.; Fang, K.; Zhu, B.; Yang, H.; Hansen, T. W.; Wagner, J. B.; Zhang, Z.; Gao, Y.; others Direct in situ TEM visualization and insight into the facet-dependent sintering behaviors of gold on TiO_2. *Angew. Chem* **2018**, *130*, 17069–17073.

(89) Alayyoub, B.; Cao, T.; Kwon, O.; Vohs, J.; Gorte, R.; Vojvodic, A. Ni Ingress and Egress in $SrTiO_3$ Single Crystals of Different Facets. *J. Phys. Chem. C* **2023**, *127*, 2875–2884.

(90) Du, X.; Huang, Y.; Pan, X.; Han, B.; Su, Y.; Jiang, Q.; Li, M.; Tang, H.; Li, G.; Qiao, B. Size-dependent strong metal-support interaction in TiO_2 supported Au nanocatalysts. *Nat. Commun* **2020**, *11*, 5811.

(91) Wang, J.; Yang, J.; Opitz, A. K.; Bowman, W.; Bliem, R.; Dimitrakopoulos, G.; Nenning, A.; Waluyo, I.; Hunt, A.; Gallet, J.-J.; others Tuning point defects by elastic strain modulates nanoparticle exsolution on perovskite oxides. *Chem. Mater.* **2021**, *33*, 5021–5034.

(92) Aso, R.; Hojo, H.; Takahashi, Y.; Akashi, T.; Midoh, Y.; Ichihashi, F.; Nakajima, H.; Tamaoka, T.; Yubuta, K.; Nakanishi, H.; others Direct identification of the charge state in a single platinum nanoparticle on titanium oxide. *Science* **2022**, *378*, 202–206.

(93) Farmer, J. A.; Campbell, C. T. Ceria maintains smaller metal catalyst particles by strong metal-support bonding. *Science* **2010**, *329*, 933–936.

(94) Hansen, T. W.; DeLaRiva, A. T.; Challa, S. R.; Datye, A. K. Sintering of catalytic nanoparticles: particle migration or Ostwald ripening? *Acc. Chem. Res.* **2013**, *46*, 1720–1730.

(95) Li, L.; Plessow, P. N.; Rieger, M.; Sauer, S.; Sánchez-Carrera, R. S.; Schaefer, A.; Abild-Pedersen, F. Modeling the migration of platinum nanoparticles on surfaces using a kinetic Monte Carlo approach. *J. Phys. Chem C* **2017**, *121*, 4261–4269.

(96) Zandkarimi, B.; Poths, P.; Alexandrova, A. N. When fluxionality beats size selection: acceleration of Ostwald ripening of sub-nano clusters. *Angew. Chem., Int. Ed* **2021**, *133*, 12080–12089.

(97) Zhang, C.; Michaelides, A.; King, D. A.; Jenkins, S. J. Positive charge states and possible polymorphism of gold nanoclusters on reduced ceria. *J. Am. Chem. Soc.* **2010**, *132*, 2175–2182.

(98) Campbell, C. T.; Mao, Z. Chemical potential of metal atoms in supported nanoparticles: dependence upon particle size and support. *ACS Catal.* **2017**, *7*, 8460–8466.

TOC Graphic

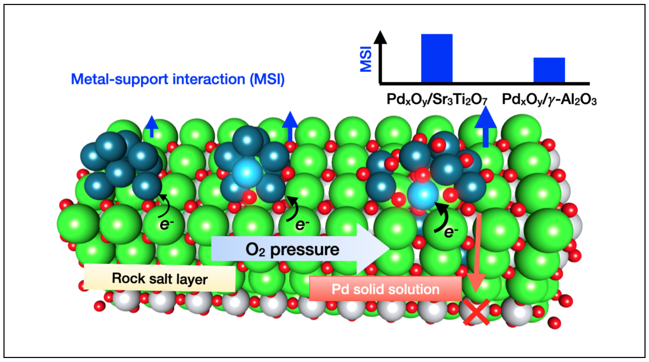
Metal-support interaction (MSI)
MSI
$Pd_xO_y/Sr_3Ti_2O_7$
$Pd_xO_y/\gamma\text{-}Al_2O_3$
e^-
e^-
e^-
O_2 pressure
Rock salt layer
Pd solid solution